Monoamine biosynthesis via a noncanonical calcium-activatable aromatic amino acid decarboxylase in psilocybin mushroom

Michael P. Torrens-Spence[1†], Chun-Ting Liu[1,2,3†], Tomáš Pluskal[1], Yin Kwan Chung[1,4] and Jing-Ke Weng[1,2*]

[1]Whitehead Institute for Biomedical Research, 455 Main Street, Cambridge, MA 02142 USA.

[2]Department of Biology, Massachusetts Institute of Technology, Cambridge, MA 02139 USA.

[3]Department of Chemistry, Massachusetts Institute of Technology, Cambridge, MA 02139 USA.

[4]Division of Life Science, Hong Kong University of Science & Technology, Clear Water Bay, Hong Kong, China

[†]Co-first authors

*Corresponding author. Email: wengj@wi.mit.edu

ABSTRACT

Aromatic L-amino acid decarboxylases (AAADs) are a phylogenetically diverse group of enzymes responsible for the decarboxylation of aromatic amino acid substrates into their corresponding aromatic arylalkylamines. AAADs have been extensively studied in mammals and plants as they catalyze the first step in the production of neurotransmitters and bioactive natural products, respectively. Unlike mammals and plants, the hallucinogenic psilocybin mushroom *Psilocybe cubensis* reportedly employs an unrelated phosphatidylserine-decarboxylase-like enzyme to catalyze L-tryptophan decarboxylation, the first step in psilocybin biosynthesis. To explore the origin of this chemistry in psilocybin mushroom, we generated the first *de novo* transcriptomes of *P. cubensis* and investigated several putative L-tryptophan-decarboxylase-like enzymes. We report the biochemical characterization of a noncanonical AAAD from *P. cubensis* (*Pc*ncAAAD) that exhibits substrate permissiveness towards L-phenylalanine, L-tyrosine, and L-tryptophan, as well as chloro-tryptophan derivatives. The crystal structure of *Pc*ncAAAD revealed the presence of a unique C-terminal appendage domain featuring a novel double β-barrel fold. This domain is required for *Pc*ncAAAD activity and regulates catalytic rate and thermal stability through calcium binding. *Pc*ncAAAD likely plays a role in psilocybin production in *P. cubensis* and offers a new tool for metabolic engineering of aromatic-amino-acid-derived natural products.

INTRODUCTION

Psilocybin is a psychoactive alkaloid produced by hallucinogenic mushrooms within the *Psilocybe* genus. Upon ingestion, psilocybin is dephosphorylated by alkaline phosphatases and other non-specific esterases in intestine and kidneys to yield psilocin, the active compound responsible for euphoria, visual and mental hallucinations, changes in perception, and spiritual experiences (*1*–*3*). Although psilocybin and its naturally occurring analogs are currently registered as Schedule I substances by the United States Drug Enforcement Administration (DEA) with no approved medical use, recent research has renewed interest in exploring psilocybin as a therapeutic agent to treat severe psychiatric disorders, including addiction (*4*), obsessive-compulsive disorder (*5*), and depression (*6*, *7*). Indeed, a total of sixteen clinical trials are currently underway to establish clinical applications of psilocybin (*8*). The biosynthetic pathway of psilocybin has been proposed for decades (*9*), however, the requisite genes and the reaction order of their corresponding enzymes have only recently been elucidated (*10*). In this pathway, psilocybin is derived from L-tryptophan by a gene cluster encoding four biosynthetic enzymes, namely L-tryptophan decarboxylase (TDC) PsiD, tryptamine 4-hydroxylase PsiH, 4-hydroxytryptamine kinase PsiK and norbaeocystin N-methyltransferase PsiM (**Figure S1**). The evolutionary histories of PsiH, PsiK and PsiM are well understood as they belong to the extensively studied cytochrome P450 (InterPro accession number: IPR001128), kinase-like domain (IPR011009) and S-adenosyl-L-methionine-dependent methyltransferase (IPR029063) superfamilies, respectively. Conversely, the evolutionary origin of PsiD remains enigmatic, as it represents a new class of fungal TDCs homologous to phosphatidylserine decarboxylases (IPR003817) (*11*–*13*). It appears that in psilocybin mushroom, L-tryptophan decarboxylation is

catalyzed by a neofunctionalized phosphatidylserine decarboxylase-like enzyme rather than the pyridoxal 5'-phosphate (PLP)-dependent aromatic L-amino acid decarboxylases (AAADs, IPR010977) typically responsible for arylalkylamine production in other kingdoms of life (*14*–*17*).

AAADs have been extensively studied in mammals as L-3,4-dihydroxyphenylalanine (L-DOPA) decarboxylase catalyzes the first step in the biosynthesis of monoamine neurotransmitters (*18*). Unlike the singular mammalian gene, the AAAD family in plants has undergone extensive radiation to produce paralogous TDC, tyrosine decarboxylase (TyDC) and acetaldehyde synthase (AAS) genes (*19*–*23*). The resulting variations in substrate selectivity and catalytic mechanisms enable individual plant AAADs to operate at distinct positions on the interface of primary and specialized metabolism. Biochemical transformations catalyzed by AAADs commit amino acid substrates into the biosynthesis of numerous important natural products, including monoterpenoid indole alkaloids, benzylisoquinoline alkaloids, and aromatic acetaldehyde derivatives. Unlike mammals and plants, AAADs in fungi have received little attention despite their purported role in the biosynthesis of melanin and alkaloids such as bufotenine and communesin (*24*, *25*). To the best of our knowledge, *Ceriporiopsis subvermispora* TDC (*Cs*TDC) is the only cloned and biochemically characterized fungal AAAD to date (*26*). Curiously, although AAAD homologs and even TDCs are present in fungi, *Psilocybe cubensis* has achieved a parallel means of tryptophan decarboxylation through PsiD. In this study, we investigated several putative L-tryptophan-decarboxylation-catalyzing enzymes in *P. cubensis*, and identified a calcium-activatable noncanonical AAAD (*Pc*ncAAAD), which likely mediates an alternative route to psilocybin biosynthesis from L-tryptophan in psilocybin mushroom.

RESULTS AND DISCUSSION

Phylogenetic analysis of type II PLP decarboxylase family proteins from *P. cubensis*

To investigate potential L-tryptophan-decarboxylation-catalyzing enzymes in psilocybin mushroom, we generated *P. cubensis de novo* transcriptome datasets from both mycelia and fruiting body tissues. Four type II PLP decarboxylase-encoding genes were identified from the *P. cubensis* transcriptomes. The evolutionary relationships of these *P. cubensis* enzymes were investigated together with representative type II PLP decarboxylases from 22 sequenced agaricomycetes species (**Figure 1A**). This analysis revealed that two *P. cubensis* enzymes, *Pc*GAD1 and *Pc*GAD2, belong to the L-glutamate decarboxylase (GAD) family, whereas the other two fall into canonical and noncanonical clades of the AAAD family.

The GAD clade contains the previously characterized *Saccharomyces cerevisiae* GAD (*27*), to which *Pc*GAD1 and *Pc*GAD2 share 48% and 49% amino acid sequence identity, respectively. Like *P. cubensis,* most of the sequenced agaricomycetes species also contain two GAD-like genes, suggesting an ancestral gene duplication event before the agaricomycetes class radiated. The second clade, annotated as the AAAD clade due to the inclusion of the characterized *Cs*TDC (*26*), contains a single *P. cubensis* enzyme with probable substrate selectivity towards L-aromatic amino acid substrates. This enzyme could plausibly accommodate L-tryptophan as a substrate; however, the substitution of a catalytic-loop tyrosine to phenylalanine at residue 329 suggests that this enzyme likely functions as an AAS rather than a canonical decarboxylation-catalyzing AAAD (**Figure S2**) (*28*). Whereas both the AAAD and GAD clades contain genes with characterized enzymatic

activities, proteins that fall into the noncanonical AAAD (ncAAAD) clade are much longer in sequence and have not been functionally characterized. Sequence analysis of the single *P. cubensis* ncAAAD clade protein, revealed that the N-terminus (Met^{1} - Val^{705}) belongs to the PLP-dependent decarboxylase (IPR002129) family, whereas the C-terminus (Met^{706} - Lys^{1013}) has no homology to any characterized protein.

Tissue-specific transcript abundance of *P. cubensis* type II PLP decarboxylase-encoding genes

To assess the putative role of these newly identified *P. cubensis* type II PLP decarboxylases in psilocybin biosynthesis, the abundance of the mycelia and fruiting-body transcripts were quantified and ranked by transcript-per-million (TPM) values using RSEM software and in-house scripts (*29*). *PcncAAAD* is amongst the most highly expressed genes with a TPM rank of 241 out of the 13,672 total fruiting body transcripts. As one of the top 2% most highly expressed genes, *PcncAAAD* surpassed the transcript abundance of the previously characterized psilocybin biosynthetic genes (**Table S1 and Figure S3**). In comparison, *PcGAD1, PcGAD2,* and *Pc*AAS are much less abundant with TPM rankings in fruiting body of 5029, 7196 and 9715, respectively. *PcGAD1* and *PcGAD2* show marginally higher transcript abundance in the mycelium (**Figure S4**), while *PcAAS and PcncAAAD* display tissue-specific expression patterns similar to those of the known psilocybin biosynthetic genes. Given the unusually high expression level of *PcncAAAD* and the fact that psilocybin is known to accumulate mostly in the fruiting body of psilocybin mushrooms (*30*), we hypothesized that *PcncAAAD* likely plays a role in psilocybin biosynthesis.

Biochemical functions of three *P. cubensis* type II PLP decarboxylase family proteins

To confirm their biochemical functions, the activities of the *P. cubensis* type II PLP decarboxylases were assessed *in vitro* with recombinant protein biochemistry or *in vivo* through heterologous expression in transgenic yeast followed by metabolic profiling. *Pc*AAS was first investigated since it is most closely related to the previously described *Cs*TDC. As predicted by the presence of the catalytic-loop Tyr-to-Phe substitution at residue 329, recombinant *Pc*AAS exhibits AAS activity with an apparent substrate selectivity towards L-DOPA (**Figure S5**). Accordingly, this enzyme was annotated as *P. cubensis* 3,4-dihydroxyphenylacetaldehyde synthase (*Pc*DHPAAS). Biochemically, *Pc*DHPAAS displays a similar activity to that of the insect chitin-based cuticle development α-methyl DOPA resistant (AMD-r) protein (*31*). Since chitin is a key structural component in both the exoskeleton of arthropods and the cell wall of fungi, *Pc*DHPAAS may serve a similar function as AMD-r in the production of dihydroxyphenylacetaldehyde from L-DOPA for crosslinking chitin.

We next characterized *Pc*GAD1, as a representative enzyme of the GAD clade. Recombinant *Pc*GAD1 was expressed, purified, and assayed against the full panel of proteinogenic L-amino acid substrates. Nevertheless, no measurable enzyme activity was detected. Inability to measure *in vitro* activity for recombinant fungal GADs has been previously reported, which was attributed to the absence of calcium and calmodulin required for the activation of GAD activity *in vivo* (*27*, *32*). To circumvent this caveat, we generated transgenic yeast expressing *Pc*GAD1, and profiled the metabolome of the resultant cells by liquid chromatography high-resolution accurate-mass mass-spectrometry (LC-HRAM-MS). The *Pc*GAD1-expressing yeast showed significantly higher accumulation of both γ-aminobutyric

acid (GABA) and its downstream catabolite, succinate, compared to the wild-type control (**Figure S6**), confirming the *in vivo* L-glutamate decarboxylation activity of *Pc*GAD1. Although GADs are ubiquitous enzymes in both fungi and plants, their exact physiological functions remain to be investigated in their native hosts (*33*). In fungi, GABA was shown to serve as an alternative nitrogen source with potential roles in pathogenicity and development (*34*, *35*).

Finally, recombinant *Pc*ncAAAD, when challenged with L-amino acid substrates, demonstrated decarboxylation activity towards L-phenylalanine, L-tyrosine and L-tryptophan (**Figure S7**). This broad substrate specificity observed in *Pc*ncAAAD is notable as plant AAADs typically display selectivity towards a single L-aromatic amino acid substrate (*14*). *Pc*ncAAAD was therefore selected for in-depth characterization as it represents a novel clade of fungal AAAD family enzymes capable of catalyzing L-tryptophan decarboxylation, the first committed step of psilocybin biosynthesis. The biochemical functions of *Pc*DHPAAS, *Pc*GAD1, and *Pc*ncAAAD are summarized in **Figure 1B**.

Enzyme kinetics of *Pc*ncAAAD

Whereas previously characterized plant AAADs principally display selectivity towards an individual substrate, recombinant *Pc*ncAAAD exhibits L-aromatic amino acid substrate permissiveness. To assess the relative substrate preference of *Pc*ncAAAD towards L-phenylalanine, L-tyrosine and L-tryptophan, we performed Michaelis-Menten kinetic assays using recombinant *Pc*ncAAAD against these three substrates in a generic NaCl-containing reaction buffer at pH 8.0 (**Table 1 and Figure S8**). *Pc*ncAAAD exhibits K_M values of 0.82 mM and 0.45 mM against L-phenylalanine and L-tryptophan, respectively, although the catalytic efficiency for L-phenylalanine

(11.80 sec^{-1} mM^{-1}) is greater than that of L-tryptophan (1.33 sec^{-1} mM^{-1}). The turnover rate and Michaelis constant towards L-tyrosine was ultimately not determined as the maximum rate of the reaction was limited by the solubility of the substrate. Although the kinetic constants could not be measured, *Pc*ncAAAD readily decarboxylates L-tyrosine with a specific activity four times that of L-tryptophan and one quarter that of L-phenylalanine at 2 mM substrate concentration.

***In vivo* characterization of *Pc*ncAAAD substrate selectivity in transgenic yeast**

*Pc*ncAAAD catalyzes decarboxylation of multiple L-aromatic amino acids into their corresponding monoamine products *in vitro*; however, the role and abundance of these specialized metabolites in *P. cubensis* remain unclear. As psilocybin mushrooms reportedly contain multiple psilocybin-like biosynthetic gene clusters (*36*), *Pc*ncAAAD may operate within one of these gene clusters in the production of psilocybin-like specialized metabolites. Due to difficulties of genetic studies in *P. cubensis,* we compared the *in vivo* product formation of *Pc*ncAAAD against that of previously described AAADs operating in known biosynthetic pathways in the context of transgenic yeast. We generated transgenic yeast overexpressing the *Catharanthus roseus* TDC (*Cr*TDC), *Papaver somniferum* TyDC (*Ps*TyDC), PsiD or *Pc*ncAAAD, and profiled the metabolome of these engineered yeast strains by LC-HRAM-MS (**Figure 2 and Figure S9**). Compared to the wild-type control, the *Pc*ncAAAD-expressing yeast ectopically accumulates tyramine, phenylethylamine, and tryptamine, confirming *Pc*ncAAAD's broad *in vivo* substrate specificity. Tyramine accumulation in yeast expressing *Pc*ncAAAD was similar to that of yeast expressing *Ps*TyDC*,* whereas ectopic tryptamine levels in the *Pc*ncAAAD, PsiD and *Cr*TDC-expressing strains are within 2-fold difference. Despite utilizing a number of L-

aromatic amino acid substrates, the *Pc*ncAAAD-expressing yeast strain displayed accumulated levels of individual monoamines comparably to those of the strains expressing substrate-specific decarboxylases.

*Pc*ncAAAD can accommodate chlorinated tryptophans as substrates

Using halogenated L-tryptophan as a precursor for the biosynthesis of halogenated monoterpene indole alkaloid in *C. roseus* has been demonstrated as a viable approach to produce novel natural product analogs (*37*). However, the poor activity of the native *Cr*TDC towards halogenated L-tryptophan acts as a metabolic bottleneck in the biosynthesis of downstream halogenated alkaloids. Consequently, the substrate permissive *Pc*ncAAAD may demonstrate utility in metabolic engineering of natural products derived from halogenated L-tryptophan. To test whether *Pc*ncAAAD can accommodate chlorinated substrates, we constructed transgenic yeast strains expressing two previously described halogenases, PyrH and RebH, that produce 5-chlorotryptophan and 7-chlorotryptophan, respectively, from L-tryptophan. The resultant chlorotryptophan then serves as the *in vivo* substrate for either *Pc*ncAAAD, PsiD or *Cr*TDC in transgenic yeast (**Figure 3A**). While *Cr*TDC displays no activity towards 5-chlorotryptophan and minimal activity towards 7-chlorotryptophan, PsiD demonstrated a level of substrate permissiveness towards both 5- and 7-chlorotryptophan (**Figure 3B**). *Pc*ncAAAD also accommodates both 5- and 7-chlorotryptophan as substrates but displays higher 7-chlorotryptamine production than PsiD. In addition to monoterpene indole alkaloid engineering, *Pc*ncAAAD may also aid in the production of halogenated psilocybin derivatives.

Overall structure of *Pc*ncAAAD

To understand the structural basis for substrate permissiveness and the function of the C-terminal appendage domain, we solved the X-ray crystal structure of *Pc*ncAAAD at 1.97 Å resolution (PDB ID: 6EBN, **Table S2**). Similar to other AAADs, *Pc*ncAAAD purifies and crystallizes as a homodimer. N-terminal (Met^{1} - Arg^{13}), C-terminal (Gly^{985} - Lys^{1013}) and loop (Ile^{765} - Arg^{770}) residues were not modeled in the final structure due to poor electron density support. In the *Pc*ncAAAD homodimer, the two lysine-pyridoxal-5'-phosphate (LLP^{443}) groups are symmetrically bound in the clefts of the monomer-monomer interface. Each individual chain is composed of the core type I aspartate aminotransferase superfamily domain (Val^{14} - Asp^{717}) (*38*) and a novel double β-barrel C-terminal appendage domain (Met^{718} - Tyr^{984}) (**Figure 4A, 4B**). The catalytic core domain, as described in other AAADs, is composed of the N-terminal, PLP-binding and C-terminal segments (**Figure S10**) (*23*, *39*). Superimposition of the core domain of *Pc*ncAAAD with its most closely related crystal structure, *Lactobacillus brevis* TyDC (*Lb*TyDC, PDB ID: 5HSJ) (*40*), demonstrates a high degree of conserved topology with a calculated RSMD of 0.34 Å (**Figure S11A**). The differences between *Lb*TyDC and the catalytic domain of *Pc*ncAAAD mainly occur on the exterior of the structure, with an additional two-stranded β-sheet (Asp^{211} - Leu^{224}) and a stretch of three inserted α-helices (Phe^{545} - Gly^{594}) in *Pc*ncAAAD (**Figure S11B**). Additionally, a helix in the *Lb*TyDC structure (Leu^{340} - Thr^{363}) adopts a loop configuration in the *Pc*ncAAAD structure (Leu^{393} - Val^{415}), in which the chain has rotated outwards towards the N-terminus and solvent shell. (**Figure S11C**).

The *Pc*ncAAAD catalytic loop (Trp^{467}-Ile^{481}), required for activity in type II PLP decarboxylases, is observed in an open conformation similar to that of the *Cr*TDC structure (**Figure S12**) (*23*). Although both the *Pc*ncAAAD and *Cr*TDC structures

adopt open conformations, the short helix in *Cr*TDC (Pro^{346} - Lys^{350}), postulated to "unlock" the initial closing motion of the catalytic loop, is displaced in the *Pc*ncAAAD structure by a distal helix (Pro^{256} - Ile^{267}) not present in *Cr*TDC (*23*). The dislocation, caused by the aforementioned insertion, protrudes the *Pc*ncAAAD catalytic loop away from the active site to form new intermolecular interactions with the other *Pc*ncAAAD monomer. The open conformations of the *Pc*ncAAAD and *Cr*TDC structures are in contrast to the closed configuration observed in *Ps*TyDC and *Hm*HDC in which the corresponding loop is sealed over the active site with the catalytic tyrosine positioned proximal to the substrate Cα (*23*, *41*). The alternative loop conformations revealed by *Pc*ncAAAD and previously reported AAAD structures inform the dynamic nature of the loop pertinent to its role in the catalytic cycle (*23*).

The C-terminal appendage domain consists of two perpendicularly stacked β-barrel repeats, each containing six β-strands followed by a downstream helix-containing loop (**Figure 4C**). Repeat 1 (Met^{718} - Leu^{833}) is distinguished from repeat 2 (Met^{834} - Tyr^{984}) as it lacks the loop insertions Ala^{891} - Gln^{907}, Tyr^{925} - Lys^{939}, and Ala^{970} - His^{976} (**Figure 4D**). The sheet topology of each β-barrel repeat has the order of 6–3–2–1–4–5-6 with 3–2–1–4 being the Greek-key motif (**Figure 4E, 4F**). Fold similarity search using the DALI server (*42*) failed to identify any known tertiary structures similar to the *Pc*ncAAAD C-terminal appendage domain, suggesting a novel topology which we named the Cuben fold after its source organism.

Each monomer of the *Pc*ncAAAD homodimer contains two metal-binding sites occupied by sodium ions derived from the crystallization buffer. Both metal-binding sites are formed cooperatively from domain or repeat structural interactions and may regulate conformational changes and allostery in *Pc*ncAAAD. The first metal-binding site, located at the boundary between domains, is composed of Gln^{629}, Ser^{632} and

Glu^{638} from the catalytic domain and Asp^{971} from repeat 2 of the C-terminal domain (**Figure 5A**). The second metal-binding site is composed of the C-terminal domain residues Glu^{824} and Asp^{825} from the Cuben-fold repeat 1 and Met^{930} of repeat 2 (**Figure 5B**). In addition to coordinating the sodium ion, the loop structure from the first metal-binding site also interacts with Gly^{478} of the catalytic loop via the carbonyl of Thr^{634}. As the R-group of Thr^{634} in turn forms a hydrogen bond with one of the metal-coordinating waters, this residue forms a link between the first metal-binding site and the catalytic loop (**Figure 5C**). Additionally, the C-terminal-domain residues Lys^{900} and Asp^{901} further engage hydrogen-bonding and electrostatic interactions with the catalytic loop residue Gln^{474}. The specific interactions between the metal-binding sites, the C-terminal appendage domain and the catalytic loop likely impact the dynamics of *Pc*ncAAAD. Since enzyme turnover requires conformational changes of the catalytic loop, metal binding could therefore influence catalysis.

Molecular docking and active site composition

To understand the catalytic mechanism, particularly substrate binding and recognition, AutoDock Vina (*43*) was used to dock the ligands L-phenylalanine, L-tyrosine, or L-tryptophan to the *Pc*ncAAAD structure with the search area defined as the space between the LLP^{443} cofactor and the catalytic-loop Tyr^{471}. Considering the binding configuration necessary for transaldimination and decarboxylation (*44*), as well as the ligand orientation of previously solved substrate-bound AAAD structures (*23*, *39*, *41*), the most probable poses for the three amino acid substrate were determined (**Figure S13A-C**). In PLP carboxy-lyases, the labile α-carbon-carboxyl bond of the ligand is required to be positioned perpendicular to the pyridine ring of the internal aldimine LLP. In this orientation, the α-carbon of the quinonoid

intermediate would be positioned out of the active site pocket and accessible to the catalytic Tyr^{471} responsible for carbanion intermediate protonation. Furthermore, since the first step of decarboxylation is a transaldimination reaction between the substrate and the PLP-bound Lys^{443}, the α-N of the amino acid substrate and the 4′-C of PLP have to come into close proximity to initiate the reaction. The distances between α-N and 4′-C atoms in our models are 4.9 Å for L-phenylalanine, 5.3 Å for L-tyrosine, and 6.5 Å for L-tryptophan, suggesting a reasonable docking orientation capable of transaldimination. L-Phenylalanine, L-tyrosine, and L-tryptophan show similar orientations in the active site with their aromatic side chains buried deep inside the active-site cavity. The substrates are anchored at their amine and carboxyl groups to the side chains of His^{295} and Tyr^{296} by two to three hydrogen bonds. The hydrophobic active site environment created by Met^{108}, Val^{131}, Ala^{132} and Lys^{443}, along with the π-π interaction of His^{107} and the aromatic substrate, likely engender the broad substrate selectivity of *Pc*ncAAAD. In the docking model, electrostatic bonds between *Pc*ncAAAD residues and the 4-hydroxyl group of L-tyrosine or the indole ring nitrogen of L-tryptophan appear to form additional stabilizing interactions.

The C-terminal appendage domain modulates *Pc*ncAAAD activity through calcium binding

To test the function of the *Pc*ncAAAD appendage domain, we expressed the N-terminal (Met^{1} - Asp^{717}) and C-terminal (Arg^{715} - Lys^{1013}) domains, either alone or together in yeast. Metabolic profiling of monoamine production in the resultant yeast strains demonstrates that the N-terminal domain alone showed little to no in *vivo* decarboxylation activity in transgenic yeast, despite the presence of the entire type I aspartate aminotransferase folding structure (**Figure 6A**). While the C-terminal

appendage domain by itself has no enzymatic activity, co-expression of N- and C-terminal domains as separate polypeptides in transgenic yeast partially recovered decarboxylase activity towards all three proteinogenic aromatic amino acid substrates. These results suggest that the C-terminal appendage is indispensable for *Pc*ncAAAD activity.

To investigate whether metal binding affects *Pc*ncAAAD activity, we first measured the activity of *Pc*ncAAAD in a series of reaction buffers containing sodium, potassium, magnesium, calcium, zinc or ferric ions (**Figure S14**). Amongst the various metal ions tested, only calcium enhanced *Pc*ncAAAD activity. Accordingly, we then determined the kinetic parameters of *Pc*ncAAAD against the three L-aromatic amino acid substrates in the presence of calcium. Notably, the catalytic rates of *Pc*ncAAAD against L-phenylalanine and L-tryptophan measured in calcium buffer are 300 and 500-fold higher than those measured in sodium buffer, respectively (**Figure 6B, Table 1-2 and Figure S15**). Finally, ThermoFluor assays (*45*) were used to measure the impact of calcium on *Pc*ncAAAD thermal stability (**Table 3 and Figure 6C**). The temperature-dependent *Pc*ncAAAD unfolding curves reveal two melting events around 51°C and 67°C in the sodium or ion-free buffer. The presence of calcium significantly increases the melting temperatures of both events, suggesting calcium binding imparts a stabilizing effect of the *Pc*ncAAAD protein. Altogether, these results suggest that the metal-binding sites observed in the *Pc*ncAAAD structure can positively regulate *Pc*ncAAAD activity through specific binding to calcium.

CONCLUSION

In this study, we characterized several type II PLP decarboxylase family enzymes identified through mining the *P.cubensis* transcriptomes. Among them, *Pc*ncAAAD was found to represent a fungal-specific clade of AAADs that likely plays a role in psilocybin biosynthesis parallel to the psilocybin biosynthetic gene cluster previously reported by Fricke et al. (*10*). In-depth biochemical characterization further shows that *Pc*ncAAAD is a broad-spectrum AAAD capable of producing tryptamine from L-tryptophan both *in vitro* and in transgenic yeast. *Pc*ncAAAD features an unusual C-terminal metal-binding domain that modulates *Pc*ncAAAD activity through calcium binding. Although US federal regulation currently precludes our ability to study the function of *Pc*ncAAAD in the context of its native host *P.cubensis*, we postulate that *Pc*ncAAAD may mediate *de novo* psilocybin biosynthesis under the control of endogenous calcium signaling and/or elevated environmental calcium concentration. The genomic context of *Pc*ncAAAD in *Psilocybe* mushrooms should inform additional players in the biosynthesis and regulation of the psilocybin pathway in psilocybin mushroom.

Although psilocybin is currently classified as a scheduled substance by many countries, its unique psychedelic activities and low toxicity profile (*46*) make it a promising therapeutic agent for treating various severe psychiatric disorders (*47*). Given its potential medicinal use, the genes discovered in our study can help future breeding or genetic modification efforts to arrive at desirable psilocybin-related traits in psilocybin mushrooms. Moreover, through the means of metabolic engineering, psilocybin and its related structural analogs, such as psilocybin with ring halogen substitutions as alluded in this study, can be produced in alternative microbial hosts, such as *E. coli* or yeast. Similar to the modern opioid pain relievers developed based

on the natural product morphine backbone, certain psilocybin analogs may contain improved pharmacological properties better suited for therapeutic uses.

METHODS

Reagents

L-amino acids, tyramine, phenylethylamine, tryptamine, γ-aminobutyric acid, succinate and PLP were purchased from Sigma-Aldrich.

RNA Isolation, Library Preparation, Transcriptome Assembly, cDNA Production, and Molecular Cloning

Total RNA was extracted from fruiting body and mycelium of *P. cubensis* using the RNeasy Mini Kit (Qiagen). RNA quality was assessed by Bioanalyzer (Agilent Technologies). For the RNA-seq experiment, strand-specific mRNA libraries were prepared using total RNA prepared separately from the fruiting body and mycelium tissue using the TruSeq Stranded mRNA Library Prep Kit (Illumina), and sequenced on a HiSeq 2000 sequencer (Illumina) in paired-end mode (PE100). Sequence FASTQ files were trimmed for sequencing adaptors using Trimmomatic (*48*) and assembled into *de novo* transcriptomes using Trinity in strand- specific mode (*49*). Gene expression statistics (TPM values) were determined by RSEM (*29*). Combining all raw sequencing reads for both tissue, a total of 39,350 unique transcripts were assembled. The combined transcriptome was evaluated by the metric of Benchmarking Universal Single-Copy Orthologs (BUSCO) (*50*) to be 97.6% complete. When using BUSCO, ‘‘fungi_odb9’’ was set as lineage and “ustilago” was set as model species. Putative coding regions were predicted using Transdecoder (*51*). Transcripts and predicted protein sequences were annotated with TPM values

and closest BLAST hits using in-house scripts. The version described in this paper is the first version, GGMK01000000. Transcriptome mining was performed on a local BLAST server (*52*). First-strand cDNAs were synthesized by RT–PCR using total RNA sample as template and the Invitrogen SuperScript III kit (Invitrogen) with the oligo(dT)20 primer. The coding sequences (CDS) of candidate genes were amplified from first-strand cDNAs by PCR using gene-specific primers (**Table S3**). RebH, RebF and PyrH were codon optimized for expression in *S. cerevisiae* and ordered as IDT gBlocks. Gibson assembly was used to ligate PCR amplicons into several base vectors. These include pHis8-4, a bacterial expression vector containing an N-terminal 8xHis tag followed by a tobacco etch virus (TEV) cleavage site for recombinant protein production in *E. coli*, and p423TEF a 2 micron plasmids (*53*) with the HIS3 auxotrophic growth markers for constitutive expression in *S. cerevisiae*. The L-tryptophan halogenation multi-gene vectors containing RebH/RebF or PyrH/RebF were constructed using the pTDH3 promoter and 2μ plasmids (*54*).

Sequence Alignment and Phylogenetic Analysis

Agaricomycetes type II PLP decarboxylase protein alignments and phylogenetic analysis were performed under MEGA7 (*55*). 77 Agaricomycetes type II PLP decarboxylases amino acid sequences were obtained from NCBI and the *P. cubensis* transcriptome. Queried NCBI species include *Agaricus bisporus* (taxid:5341), *Coniophora puteana* (taxid:80637), *Coprinopsis cinerea* (taxid:5346), *Dichomitus squalens* (taxid:114155), *Fibroporia radiculosa* (taxid:599839), *Fomitiporia mediterranea* (taxid:208960), *Fomitopsis pinicola* (taxid:40483), *Gloeophyllum trabeum* (taxid:104355), *Hebeloma cylindrosporum* (taxid:76867), *Heterobasidion annosum* (taxid:13563), *Laccaria bicolor* (taxid:29883),

Moniliophthora perniciosa (taxid:153609), *Phanerochaete chrysosporium* (taxid:5306), *Piriformospora indica* (taxid:65672), *Pleurotus ostreatus* (taxid:5322), *Postia placenta* (taxid:104341), *Punctularia strigosozonata* (taxid:202698), *Schizophyllum commune* (taxid:5334), *Serpula lacrymans* (taxid:85982), *Stereum hirsutum* (taxid:40492), *Trametes versicolor* (taxid:5325) and *Wolfiporia cocos* (taxid:81056). Phylogeny was inferred using the Maximum Likelihood method based on the JTT matrix-based model. Branches corresponding to partitions reproduced in less than 50% bootstrap replicates are collapsed in **Figure 1A**.

Metabolic Profiling by LC-HRAM-MS

Various transgenic *S. cerevisiae* BY4743 strains were generated to test the biochemical activity of candidate enzymes. 1 mL of transgenic *S. cerevisiae* culture at stationary phase was used to inoculate 50 mL of synthetic minimal medium in a shake flask. After 24 h of shaking at 30 °C, the culture was pelleted by centrifugation, washed with water, and stored at -80 °C before further processing. Yeast cells were subsequently disrupted and profiled by LC-HRAM-MS using previously described protocol (*21*). The raw data were processed and analyzed using MZmine 2 (*56*).

Recombinant Protein Production and Purification

BL21(DE3) *E. coli* containing the desired pHis8-4 expression vector were grown at 37°C in terrific broth to OD600 of 0.9, induced with 0.15 mM isopropyl-b-D-thiogalactoside (IPTG), and allowed to grow for an additional 20 h at 18 °C. Cells were harvested by centrifugation, washed with PBS (137 mM NaCl, 2.7 mM KCl, 10 mM NaH_2PO_4, and 1.8 mM KH_2PO_4), resuspended in 150 ml of lysis buffer (50 mM Tris, pH 8.0, 0.5 M NaCl, 20 mM imidazole, and 0.5 mM DTT), and lysed with five

passes through an M-110L microfluidizer (Microfluidics). The resulting crude protein lysate was clarified by centrifugation prior to Qiagen nickel–nitrilotriacetic acid (Ni–NTA) gravity flow chromatographic purification. After loading the clarified lysate, the polyhistidine-tagged recombinant protein-bound Ni–NTA resin was washed with 20 column volumes of lysis buffer and eluted with 2 column volumes of elution buffer (50 mM Tris, pH 8.0, 0.5 M NaCl, 250 mM imidazole, and 0.5 mM DTT). 1 mg of polyhistidine-tagged TEV protease was added to the eluted protein, followed by dialysis at 4°C for 16 h in dialysis buffer (50 mM Tris, pH 8.0, 0.1 M NaCl, 20 mM imidazole, and 2 mM DTT). After dialysis, protein solution was then passed through Ni–NTA resin to remove uncleaved protein and TEV. The recombinant protein was further purified by gel filtration on a fast protein liquid chromatography system (GE Healthcare Life Sciences). The principal peaks were either flash frozen in storage buffer (20 mM Tris, pH 8.0, 25 mM NaCl, and 0.5 mM DTT) or further washed to remove metal ions. To do so, the buffer of the purified enzyme was exchanged with chelating buffer (50 mM imidazole pH 8.0, 5 mM crown ether, 5 mM EDTA and 2 mM DTT) and then metal-ion-free storage buffer (25 mM Tris pH 7.5, 0.2 mM PLP and 2 mM DTT) using an amicon ultra-S15 centrifugal filter unit with ultracel-30 membrane (EMD Millipore). After flash freezing, the concentration of the recombinant protein was subsequently evaluated by image densitometric against a standard curve of bovine serum albumin standards (*57*).

Enzyme Assays

The AAS activity and substrate selectivity of the *Pc*DHPAAS was measured through the detection of the hydrogen peroxide co-product using the Pierce Quantitative Peroxide Assay Kit (Pierce) against a standard curve of hydrogen peroxide.

*Pc*ncAAAD enzyme was initially challenged in 200 µL reactions against 0.2 mM L-phenylalanine, L-tyrosine or L-tryptophan in 20 mM Tris, pH 8.0, 25 mM NaCl, and 0.5 mM DTT. Reactions were started with addition of 10 µg recombinant enzyme, incubated at 30 ˚C for 10 min, and quenched with addition of 200 µL of methanol. The reaction mixture was centrifuged and the supernatant was analyzed by LC-MS. Ten microliters of reaction mixture was analyzed by an Ultimate 3000 liquid chromatography system (Dionex) equipped with a 150 mm C18 Column (Kinetex 2.6 µm silica core shell C18 100 Å pore, Phenomenex) and coupled to an UltiMate 3000 diode-array detector (DAD) in-line UV-Vis spectrophotometer (Dionex) and a TSQ Quantum Access MAX triple-quadrupole mass spectrometer (Thermo-Scientific). Aromatic amino acids and their corresponding monoamine products were separated through gradient elution of water (0.1% formic acid) and acetonitrile (0.1% formic acid). L-tryptophan, tryptamine, L-phenylalanine, and phenylethylamine were detected by selected reaction monitoring (SRM) method. Alternative means of separation and detection were employed to measure the decarboxylation of L-tyrosine. L-tyrosine and tyramine elute at the same retention time using the aforementioned method and L-tyrosine displays in-source fragmentation to produce tyramine. Consequently, L-tyrosine and tyramine were detected by UV absorbance at 280 nm using ion-pairing isocratic LC-UV method as previously described (*21*). Analytical standards were used to confirm the formation of products. When examining the *Pc*ncAAAD metal-ion dependence, aliquots of recombinant protein washed with chelators (crown ether and EDTA) and stored in salt free buffer were incubated with substrate and 10 mM NaCl, $CaCl_2$, KI, $MgSO_4$, $ZnCl_2$, or $Fe(NO_3)_3$.

Kinetic characterization

Kinetic characterization of *Pc*ncAAAD was conducted in 100 µL reaction volume of either sodium buffer (50 mM Tris pH 8.0 and 30 mM NaCl) or calcium buffer (50 mM Tris pH 8.0 and 30 mM calcium acetate) containing substrate concentrations from 0.3 µM to 5 mM. Reactions in sodium buffer were started with the addition of 30 µg metal-ion-free recombinant enzyme, whereas 2 µg metal-ion-free recombinant enzyme was used for reactions in calcium buffer. Reactions were incubated at 25 °C for 10 min and quenched with the addition of 100 µL of methanol. After clarification, samples were then analyzed by LC-HRAM-MS using the previously described ZIC-pHILIC method (*21*). Product formation was calculated against a standard curves of authentic standards. Kinetic constants such as K_M and k_{cat} were determined by fitting raw data to the Michaelis-Menten equation using the nonlinear regression function in Prism (version 7.0).

ThermoFluor assays

In individual wells of a 384-well plate, 20 µg of enzyme premixed with 150× SYPRO® Orange dye was mixed with buffer (25 mM Tris pH 7.5, containing 8 mM NaCl, 8 mM $CaCl_2$ or no additional salt as a control) to reach a final reaction volume of 10 µL. LightCycler® 480 was used to measure fluorescence intensities using excitation at 480 nm and emission at 575 nm over a temperature ramp of 20 °C to 85 °C at a rate of 0.06 °C per second. The protein melting temperatures (Tm1 and Tm2) were determined from the peaks of the negative first derivative curve of the fluorescence signal, conducted and measured in sextuplicate.

Protein Crystallization

*Pc*ncAAAD crystals were grown by hanging drop vapor diffusion at 4 °C. The initial drop contains 2 µL of 10 mg/mL protein mixed with 1 µL of reservoir solution of 3.5 M sodium formate, pH 7.0. Crystals were cryoprotected by transferring to a reservoir solution plus an additional 25% glycerol. Single crystals were mounted in a cryoloop and flash-frozen in liquid nitrogen.

X-ray Diffraction and Structure Determination

X-ray diffraction data were collected at beamlines 24-ID-C of the Advanced Photon Source at Argonne National Laboratory for *Pc*ncAAAD crystals. Diffraction intensities were indexed and integrated with iMosflm and scaled with Scala under CCP4. The molecular replacement model of *Pc*ncAAAD was generated using Robetta (*58*) using the *Lb*TyDC (PDB ID: 5HSJ) as the template (*40*). The molecular replacement solution of *Pc*ncAAAD was determined using Molrep (*59*). The C-terminal domain was subsequently built both manually in Coot and automatically using phenix autobuild (*60*). Structural refinement was performed with Refmac 5.2 (*61*) and other Phenix programs (*62*).

Molecular Docking

All docking calculations were accomplished with AutoDock Vina 1.1.2 (*43*). The active site was defined by the space between PLP and the catalytic tyrosine. The parameters used to set the grid box dimensions and center were: center_x = 28.97; center_y = 22.00; center_z = 26.51; size_x = 25; size_y = 25; size_z = 25.

Supporting Information

Accession Codes

The sequences of *P. cubensis* genes reported in this article have been deposited in NCBI GenBank under the following accession numbers: PsiD (P0DPA6), PsiH (P0DPA7), PsiK (P0DPA8), PsiM (P0DPA9), *Pc*GAD1 (MH710579), *Pc*GAD2 (MH710580), *Pc*ncAAAD (MH710581), *Pc*DHPAAS (MH710582). The raw RNA-Seq reads have been deposited in NCBI SRA (SRR7028478 and SRR7028479). The *de novo* transcriptomes assembled from the raw reads have been deposited in NCBI TSA (GGMK00000000). The atomic coordinates and structure factors of *Pc*ncAAAD has been deposited in the Protein Data Bank (6EBN).

Author Information

Corresponding Author

Emai: wengj@wi.mit.edu

ORCID

Michael P. Torrens-Spence: 0000-0003-2644-1712

Chun-Ting Liu: 0000-0003-3996-5064

Tomáš Pluskal: 0000-0002-6940-3006

Yin Kwan Chung: 0000-0003-2868-8508

Jing-Ke Weng: 0000-0003-3059-0075

Author Contribition

M.P.T.S. and J.K.W. designed the research. M.P.T.S., C.T.L. and Y.K.C. performed all experiments. T.P. assisted with transcriptome assembly and metabolomics

analysis. M.P.T.S. and C.T.L. analysed and interpreted data. M.P.T.S., C.T.L. and J.K.W. wrote the paper.

Funding

This work was supported by grants from the Richard and Susan Smith Foundation (J.K.W), the Family Larsson-Rosenquist Foundation (J.K.W), the Pew Scholars Program in the Biomedical Sciences (J.K.W), the Searle Scholars Program (J.K.W), and the National Science Foundation (CHE-1709616, J.K.W.). T.P. is a Simons Foundation Fellow of the Helen Hay Whitney Foundation. This work is based upon research conducted at the Northeastern Collaborative Access Team beamlines, which are funded by the National Institute of General Medical Sciences from the National Institutes of Health (P30 GM124165). The Pilatus 6M detector on 24-ID-C beam line is funded by a NIH-ORIP HEI grant (S10 RR029205). This research used resources of the Advanced Photon Source, a U.S. Department of Energy (DOE) Office of Science User Facility operated for the DOE Office of Science by Argonne National Laboratory under Contract No. DE-AC02-06CH11357.

Notes

The Weng Lab of the Whitehead Institute holds Schedule I permits from the DEA and Massachusetts Controlled Substances Registration (MCSR) to carry out experiments involving psilocybin, psilocin, and N,N-dimethyltryptamine. J.K.W. is a co-founder, a member of the Scientific Advisory Board, and a shareholder of DoubleRainbow Biosciences, which develops biotechnologies related to natural products.

ACKNOWLEDGEMENTS

We thank Gerald Fink for providing yeast strains and expression vectors used in this study and Weng lab members for helpful discussion and support.

TABLES

Table 1. The kinetic parameters of *Pc*ncAAAD towards L-phenylalanine and L-tryptophan in 50 mM Tris pH 8.0 and 30 mM NaCl reaction buffer.

	k_{cat} (sec^{-1})	K_M (mM)	k_{cat} / K_M (sec^{-1} mM^{-1})
L-phenylalanine	**9.68 ± 0.28**	**0.82 ± 0.07**	**11.80**
L-tryptophan	**0.60 ± 0.06**	**0.45 ± 0.16**	**1.33**

Table 2. The kinetic parameters of *Pc*ncAAAD towards L-phenylalanine and L-tryptophan in 50 mM Tris pH 8.0 and 30 mM calcium acetate reaction buffer.

	k_{cat} (sec^{-1})	K_M (mM)	k_{cat} / K_M (sec^{-1} mM^{-1})
L-phenylalanine	**3044.00 ± 263.80**	**0.78 ± 0.21**	**3902.56**
L-tryptophan	**255.40 ± 16.23**	**0.36 ± 0.09**	**709.44**

Table 3. Melting temperatures Tm1 and Tm2 of *Pc*ncAAAD in ion-free, sodium or calcium containing buffers measured in sextuplicate.

***Pc*ncAAAD**	**Tm1 (°C)**	**Tm2 (°C)**
Ion-free buffer	**50.94 ± 0.42**	**67.30 ± 0.39**
10 mM Na^+	**50.71 ± 0.99**	**66.29 ± 0.24**
10 mM Ca^{2+}	**54.27 ± 0.19**	**69.41 ± 0.03**

FIGURES

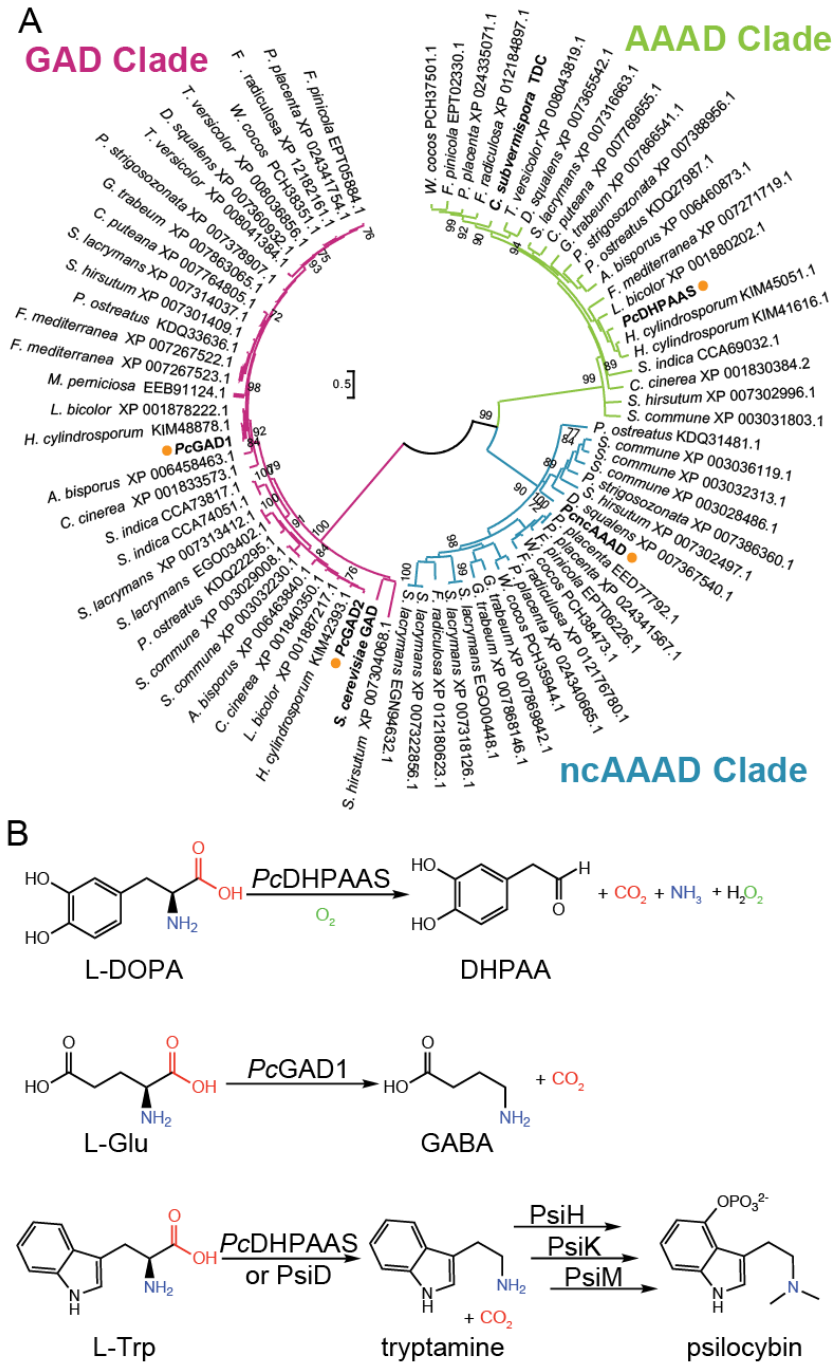

Figure 1. Phylogeny of Agaricomycetes type II PLP-dependent decarboxylases and the biochemical reactions catalyzed by *P. cubensis* AAAD enzymes characterized in this study. (A) A maximum likelihood (ML) phylogeny of Agaricomycetes type II PLP-dependent decarboxylases. Bootstrap values that are greater than 70 are displayed at the tree nodes. The three major clades are annotated as AAADs (green),

ncAAADs (blue) and GADs (purple) based on the phylogenetic pattern and functional characterization. Four genes from *P. cubensis* together with *S. cerevisiae* GAD and *C. subvermispora* TDC are shown in bold. Genes from *P. cubensis* are noted with orange dots. *C. subvermispora* TDC is the only characterized fungal AAAD with a known sequence prior to this study. *S. cerevisiae* does not belong to Agaricomycetes, but *S. cerevisiae* GAD is included here to help annotate the major clades. The average intra-clade pairwise protein sequence identity for the GAD, AAAD and ncAAAD clades are 43.5%, 54.1% and 38.0%, respectively, whereas the average pairwise protein sequence identity between two type II PLP decarboxylases from different clades is less than 23%. The scale bar measures evolutionary distances in substitutions per amino acid is shown. (B) The catalytic functions of *Pc*DHPAAS, *Pc*GAD1, PsiD and *Pc*ncAAAD. *Pc*ncAAAD can also decarboxylate L-phenylalanine and L-tyrosine.

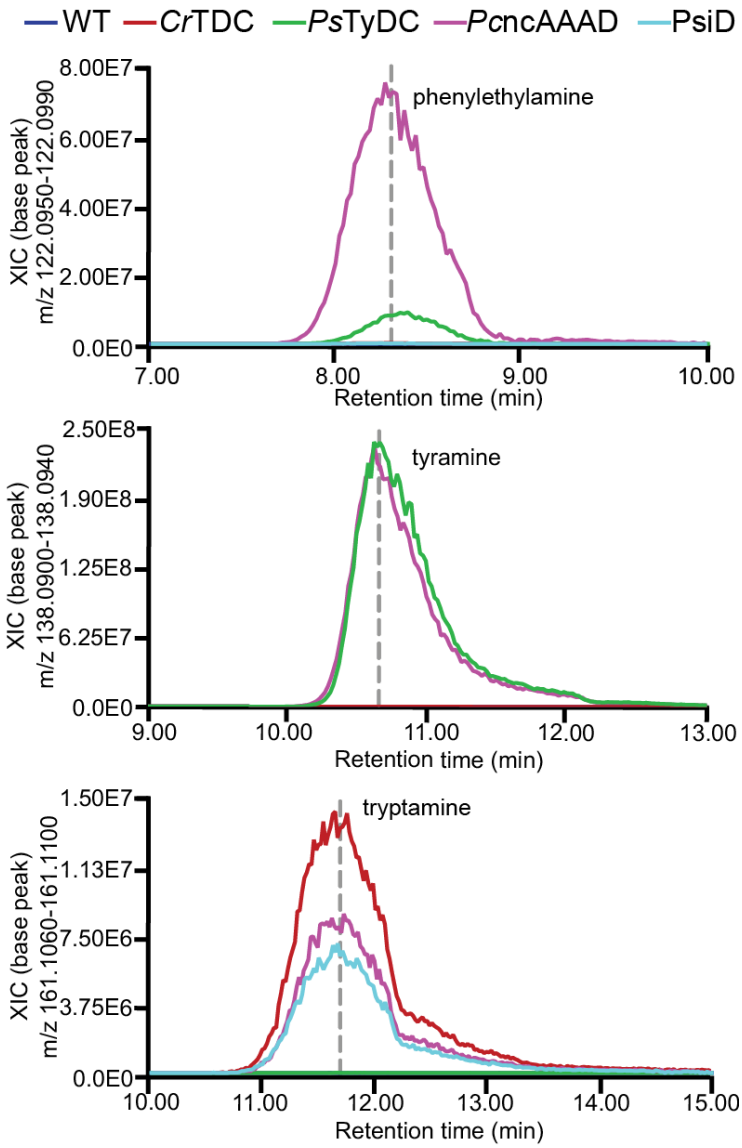

Figure 2. Relative *in vivo* AAAD activities of wild-type yeast (WT) and engineered yeast strains expressing *Cr*TDC, *Ps*TyDC, *Pc*ncAAAD or PsiD. Various type II PLP decarboxylases are constitutively expressed in yeast. The resulted yeast cell extracts were analyzed by LC-HRAM-MS. The extracted ion chromatograms (XICs) for monoamine products derived from three proteinogenic aromatic amino acids are displayed.

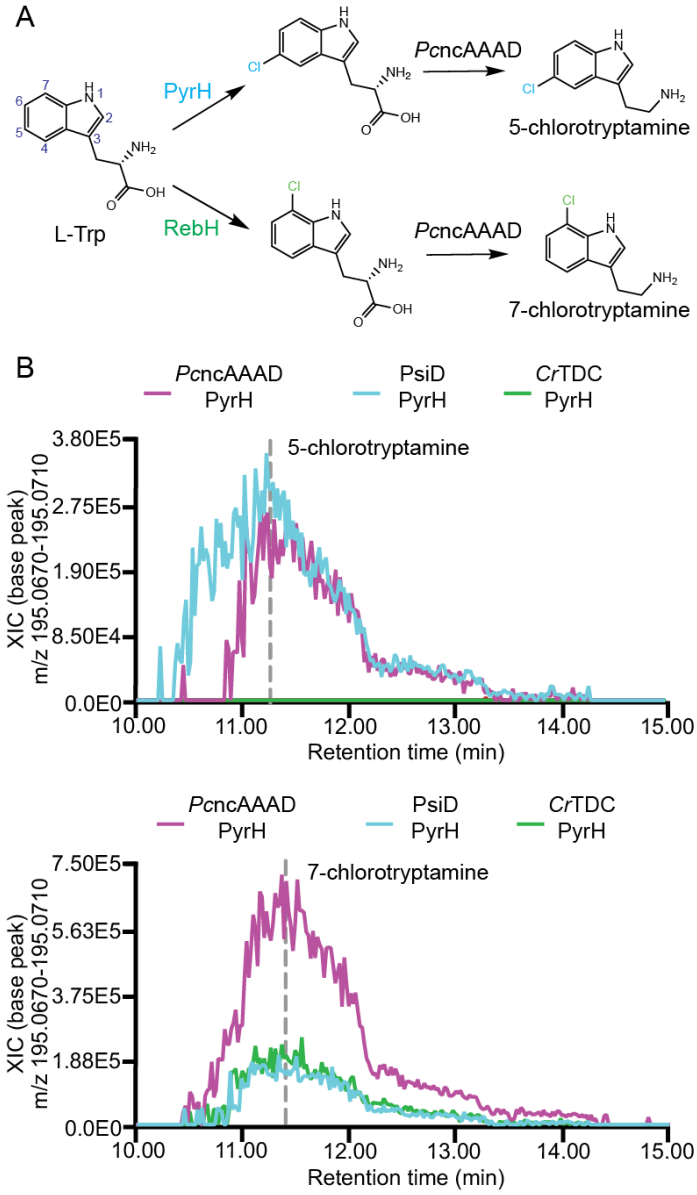

Figure 3. *Pc*ncAAAD can accommodate 5- and 7-chlorotryptophan as substrates. (A) 5- and 7-chlorotryptophan were generated from tryptophan by heterologous expression of PyrH and RebH in transgenic yeast, and served as the substrates for *Pc*ncAAAD. (B) Relative *in vivo* production of 5- and 7-chlorotryptamine in yeast expressing either *Pc*ncAAAD, PsiD, or *Cr*TDC together with PyrH (top) or RebH (bottom).

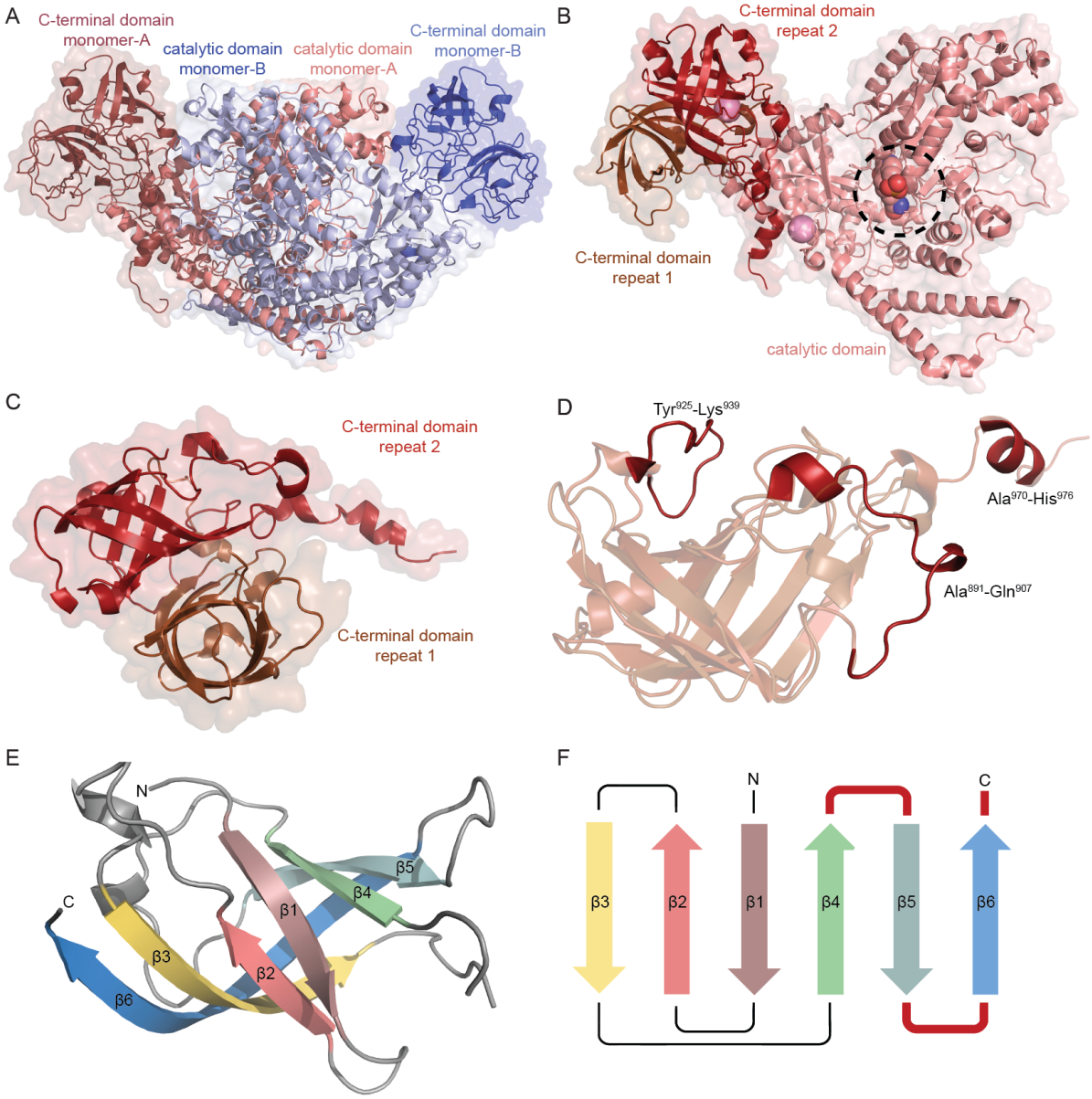

Figure 4. Architecture of *Pc*ncAAAD. (A) Cartoon and surface representation of the dimmeric *Pc*ncAAAD. (B) Cartoon and surface representation of monomeric *Pc*ncAAAD. The sodium ions are shown as pink spheres, and the active-site LLP^{443} is highlighted by a dotted circle. (C) Cartoon and surface representation of the novel *Pc*ncAAAD C-terminal appendage domain, named as the Cuben fold, composed of two perpendicular β-barrel repeats. Repeat 1 and 2 are colored in brown and fire brick red, respectively. (D) Superimposition of repeat 1 and repeat 2 showing conservation of the β-barrel fold. The loop insertions that are only present in repeat 2

are emphasized and annotated. (E) Cartoon representation of the repeat 1 six-stranded β-barrel fold. (F) Topology map of repeat 1 from the Cuben fold. The loop insertions unique to repeat 2 are displayed as red lines.

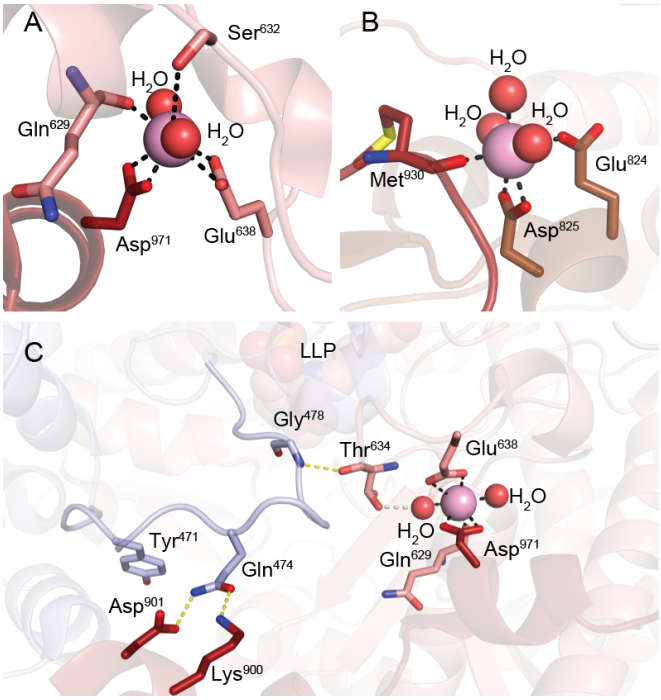

Figure 5. The two metal-binding sites observed in *Pc*ncAAAD structure and a possible mechanism of metal binding allostery. (A) The first metal ion binding site consists of two waters, three residues (Gln^{629}, Ser^{632} and Glu^{638}) from the catalytic domain (salmon) and a single residue (Asp^{971}) from repeat 2 of the C-terminal appendage domain (fire brick red). (B) The second metal ion binding site consists of three waters, two repeat-1 residues (Glu^{824} and Asp^{825}) and one repeat-2 residue (Met^{930}) of the Cuben domain. Repeat 1 and repeat 2 are colored in brown and fire brick red, respectively. (C) The catalytic loop of the other monomer (light blue) engages in electrostatic interactions, show as yellow dotted lines, with Lys^{900} and Asp^{901} from repeat 2 of the C-terminal appendage domain and Thr^{634} of the catalytic domain. The R-group of Thr^{634} in turn forms a hydrogen bond with one of the metal-coordinating water molecules. The catalytic domain and repeat 2 of the C-terminal appendage domain are rendered in salmon and fire brick red, respectively. LLP is displayed as spheres at 1.0X scale. Waters and the sodium ion are displayed as spheres at 0.5X scale and are colored in red and light pink, respectively.

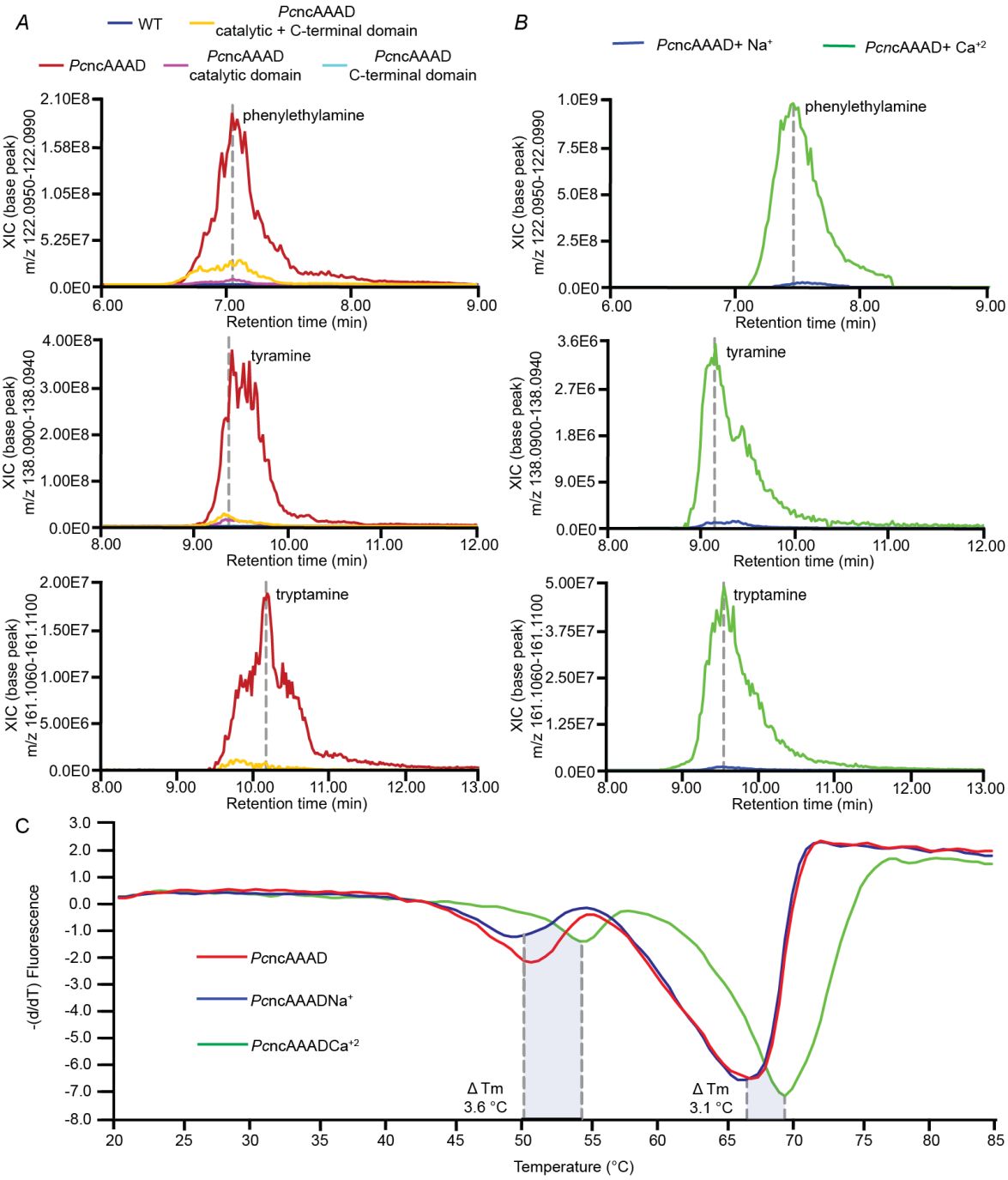

Figure 6. The role of C-terminal appendage domain and calcium binding in modulating *Pc*ncAAAD activity and thermostability. (A) *In vivo* monoamine production in transgenic yeast strains expressing full-length *Pc*ncAAAD, *Pc*ncAAAD N-terminal domain, *Pc*ncAAAD C-terminal domain, or *Pc*ncAAAD N- and C-terminal

domains as separate polypeptides. The extracted ion chromatograms (XICs) for monoamine products derived from three L-aromatic amino acids are displayed. (B) Relative *in vitro* production of monoamines by *Pc*ncAAAD in sodium buffer (50 mM Tris pH 8.0 and 30 mM NaCl) or calcium buffer (50 mM Tris pH 8.0 and 30 mM calcium acetate). (C) ThermoFluor assay demonstrates the effect of metal binding on the thermostability of *Pc*ncAAAD. The first derivative of fluorescence versus temperature plot is shown. The melting temperature differences between samples measured in sodium and calcium buffers are shaded in blue.

REFERENCES

1. Nichols, D. E. (2004) Hallucinogens, *Pharmacol. Ther. 101*, 131–181.
2. Horita, A., and Weber, L. J. (1961) The enzymic dephosphorylation and oxidation of psilocybin and psilocin by mammalian tissue homogenates, *Biochem. Pharmacol. 7*, 47–54.
3. Horita, A., and Weber, L. J. (1962) Dephosphorylation of psilocybin in the intact mouse, *Toxicol. Appl. Pharmacol. 4*, 730–737.
4. Johnson, M. W., Garcia-Romeu, A., Cosimano, M. P., and Griffiths, R. R. (2014) Pilot study of the 5-HT2AR agonist psilocybin in the treatment of tobacco addiction, *J. Psychopharmacol. 28*, 983–992.
5. Moreno, F. A., Wiegand, C. B., Keolani Taitano, E., and Delgado, P. L. (2006) Safety, Tolerability, and Efficacy of Psilocybin in 9 Patients With Obsessive-Compulsive Disorder, *J. Clin. Psychiatry 67*, 1735–1740.
6. Carhart-Harris, R. L., Bolstridge, M., Day, C. M. J., Rucker, J., Watts, R., Erritzoe, D. E., Kaelen, M., Giribaldi, B., Bloomfield, M., Pilling, S., Rickard, J. A., Forbes, B., Feilding, A., Taylor, D., Curran, H. V., and Nutt, D. J. (2018) Psilocybin with psychological support for treatment-resistant depression: six-month follow-up, *Psychopharmacology 235*, 399–408.
7. Carhart-Harris, R. L., Bolstridge, M., Rucker, J., Day, C. M. J., Erritzoe, D., Kaelen, M., Bloomfield, M., Rickard, J. A., Forbes, B., Feilding, A., Taylor, D., Pilling, S., Curran, V. H., and Nutt, D. J. (2016) Psilocybin with psychological support for treatment-resistant depression: an open-label feasibility study, *Lancet Psychiatry 3*, 619–627.
8. Search of: psilocybin | Recruiting, Active, not recruiting Studies - List Results - ClinicalTrials.gov.
9. Agurell, S., Nilsson, J. L. G., Liaaen-Jensen, S., Schwieter, U., and Paasivirta, J. (1968) Biosynthesis of Psilocybin. Part II. Incorporation of Labelled Tryptamine Derivatives, *Acta Chem. Scand. 22*, 1210–1218.
10. Fricke, J., Blei, F., and Hoffmeister, D. (2017) Enzymatic Synthesis of Psilocybin, *Angew. Chem. Int. Ed Engl. 56*, 12352–12355.
11. Choi, J.-Y., Duraisingh, M. T., Marti, M., Ben Mamoun, C., and Voelker, D. R. (2015) From Protease to Decarboxylase, *J. Biol. Chem. 290*, 10972–10980.
12. Reynolds, H. T., Vijayakumar, V., Gluck-Thaler, E., Korotkin, H. B., Matheny, P. B., and Slot, J. C. (2017) Horizontal gene cluster transfer increased hallucinogenic mushroom diversity.
13. Trotter, P. J., Pedretti, J., Yates, R., and Voelker, D. R. (1995) Phosphatidylserine decarboxylase 2 of Saccharomyces cerevisiáe. Cloning and mapping of the gene, heterologous expression, and creation of the null allele, *J. Biol. Chem. 270*, 6071–6080.
14. Facchini, P. J., Huber-Allanach, K. L., and Tari, L. W. (2000) Plant aromatic L-amino acid decarboxylases: evolution, biochemistry, regulation, and metabolic engineering applications, *Phytochemistry 54*, 121–138.
15. Bertoldi, M. (2014) Mammalian Dopa decarboxylase: structure, catalytic activity and inhibition, *Arch. Biochem. Biophys. 546*, 1–7.
16. Han, Q., Ding, H., Robinson, H., Christensen, B. M., and Li, J. (2010) Crystal structure and substrate specificity of Drosophila 3,4-dihydroxyphenylalanine decarboxylase, *PLoS One 5*, e8826.
17. Koyanagi, T., Nakagawa, A., Sakurama, H., Yamamoto, K., Sakurai, N., Takagi,

Y., Minami, H., Katayama, T., and Kumagai, H. (2012) Eukaryotic-type aromatic amino acid decarboxylase from the root colonizer Pseudomonas putida is highly specific for 3,4-dihydroxyphenyl-L-alanine, an allelochemical in the rhizosphere, *Microbiology 158*, 2965–2974.
18. Muñoz, P., Huenchuguala, S., Paris, I., and Segura-Aguilar, J. (2012) Dopamine oxidation and autophagy, *Parkinsons Dis. 2012*, 920953.
19. Facchini, P. J., and De Luca, V. (1994) Differential and tissue-specific expression of a gene family for tyrosine/dopa decarboxylase in opium poppy, *J. Biol. Chem. 269*, 26684–26690.
20. Zhao, J., Missihoun, T. D., and Bartels, D. (2017) The role of Arabidopsis aldehyde dehydrogenase genes in response to high temperature and stress combinations, *J. Exp. Bot. 68*, 4295–4308.
21. Torrens-Spence, M. P., Pluskal, T., Li, F.-S., Carballo, V., and Weng, J.-K. (2018) Complete Pathway Elucidation and Heterologous Reconstitution of Rhodiola Salidroside Biosynthesis, *Mol. Plant 11*, 205–217.
22. Noé, W., Mollenschott, C., and Berlin, J. (1984) Tryptophan decarboxylase from Catharanthus roseus cell suspension cultures: purification, molecular and kinetic data of the homogenous protein, *Plant Mol. Biol. 3*, 281–288.
23. Torrens-Spence, M. P., Chiang, Y.-C., Smith, T., Vicent, M. A., Wang, Y., and Weng, J.-K. (2018) Structural basis for independent origins of new catalytic machineries in plant AAAD proteins.
24. Niedens, B. R., Parker, S. R., Stierle, D. B., and Stierle, A. A. (1999) First Fungal Aromatic L-Amino Acid Decarboxylase from a Paclitaxel-Producing Penicillium raistrickii, *Mycologia 91*, 619.
25. Xu, W., Gavia, D. J., and Tang, Y. (2014) Biosynthesis of fungal indole alkaloids, *Nat. Prod. Rep. 31*, 1474–1487.
26. Kalb, D., Gressler, J., and Hoffmeister, D. (2016) Active-Site Engineering Expands the Substrate Profile of the Basidiomycete L-Tryptophan Decarboxylase CsTDC, *Chembiochem 17*, 132–136.
27. Coleman, S. T., Fang, T. K., Rovinsky, S. A., Turano, F. J., and Moye-Rowley, W. S. (2001) Expression of a glutamate decarboxylase homologue is required for normal oxidative stress tolerance in Saccharomyces cerevisiae, *J. Biol. Chem. 276*, 244–250.
28. Torrens-Spence, M. P., Liu, P., Ding, H., Harich, K., Gillaspy, G., and Li, J. (2013) Biochemical evaluation of the decarboxylation and decarboxylation-deamination activities of plant aromatic amino acid decarboxylases, *J. Biol. Chem. 288*, 2376–2387.
29. Li, B., and Dewey, C. N. (2011) RSEM: accurate transcript quantification from RNA-Seq data with or without a reference genome, *BMC Bioinformatics 12*, 323.
30. Gartz, J., Allen, J. W., and Merlin, M. D. (1994) Ethnomycology, biochemistry, and cultivation of Psilocybe samuiensis Guzmán, Bandala and Allen, a new psychoactive fungus from Koh Samui, Thailand, *J. Ethnopharmacol. 43*, 73–80.
31. Vavricka, C., Han, Q., Huang, Y., Erickson, S. M., Harich, K., Christensen, B. M., and Li, J. (2011) From L-Dopa to Dihydroxyphenylacetaldehyde: A Toxic Biochemical Pathway Plays a Vital Physiological Function in Insects, *PLoS One 6*, e16124.
32. Baum, G., Lev-Yadun, S., Fridmann, Y., Arazi, T., Katsnelson, H., Zik, M., and Fromm, H. (1996) Calmodulin binding to glutamate decarboxylase is required for regulation of glutamate and GABA metabolism and normal development in plants, *EMBO J. 15*, 2988–2996.

33. Bouché, N., Lacombe, B., and Fromm, H. (2003) GABA signaling: a conserved and ubiquitous mechanism, *Trends Cell Biol. 13*, 607–610.
34. Solomon, P. S., and Oliver, R. P. (2001) Evidence that γ-aminobutyric acid is a major nitrogen source during Cladosporium fulvum infection of tomato, *Planta 214*, 414–420.
35. Mead, O., Thynne, E., Winterberg, B., and Solomon, P. S. (2013) Characterising the role of GABA and its metabolism in the wheat pathogen Stagonospora nodorum, *PLoS One 8*, e78368.
36. Awan, A. R., Winter, J. M., Turner, D., Shaw, W. M., Suz, L. M., Bradshaw, A. J., Ellis, T., and Dentinger, B. (2018) Convergent evolution of psilocybin biosynthesis by psychedelic mushrooms.
37. Runguphan, W., Qu, X., and O'Connor, S. E. (2010) Integrating carbon-halogen bond formation into medicinal plant metabolism, *Nature 468*, 461–464.
38. Mehta, P. K., Hale, T. I., and Christen, P. (1991) Evolutionary Relationships among Pyridoxal Phosphate-Dependent Enzymes. In *Enzymes Dependent on Pyridoxal Phosphate and Other Carbonyl Compounds As Cofactors*, pp 35–42.
39. Burkhard, P., Dominici, P., Borri-Voltattorni, C., Jansonius, J. N., and Malashkevich, V. N. (2001) Structural insight into Parkinson's disease treatment from drug-inhibited DOPA decarboxylase, *Nat. Struct. Biol. 8*, 963–967.
40. Zhu, H., Xu, G., Zhang, K., Kong, X., Han, R., Zhou, J., and Ni, Y. (2016) Crystal structure of tyrosine decarboxylase and identification of key residues involved in conformational swing and substrate binding, *Sci. Rep. 6*, 27779.
41. Komori, H., Nitta, Y., Ueno, H., and Higuchi, Y. (2012) Structural study reveals that Ser-354 determines substrate specificity on human histidine decarboxylase, *J. Biol. Chem. 287*, 29175–29183.
42. Holm, L., and Laakso, L. M. (2016) Dali server update, *Nucleic Acids Res. 44*, W351–5.
43. Trott, O., and Olson, A. J. (2010) AutoDock Vina: improving the speed and accuracy of docking with a new scoring function, efficient optimization, and multithreading, *J. Comput. Chem. 31*, 455–461.
44. Dunathan, H. C. (1966) Conformation and reaction specificity in pyridoxal phosphate enzymes, *Proceedings of the National Academy of Sciences 55*, 712–716.
45. Semisotnov, G. V., Rodionova, N. A., Razgulyaev, O. I., Uversky, V. N., Gripas', A. F., and Gilmanshin, R. I. (1991) Study of the "molten globule" intermediate state in protein folding by a hydrophobic fluorescent probe, *Biopolymers 31*, 119–128.
46. Gable, R. S. (2004) Comparison of acute lethal toxicity of commonly abused psychoactive substances, *Addiction 99*, 686–696.
47. Carhart-Harris, R. L., and Goodwin, G. M. (2017) The Therapeutic Potential of Psychedelic Drugs: Past, Present, and Future, *Neuropsychopharmacology 42*, 2105–2113.
48. Bolger, A. M., Lohse, M., and Usadel, B. (2014) Trimmomatic: a flexible trimmer for Illumina sequence data, *Bioinformatics 30*, 2114–2120.
49. Grabherr, M. G., Haas, B. J., Yassour, M., Levin, J. Z., Thompson, D. A., Amit, I., Adiconis, X., Fan, L., Raychowdhury, R., Zeng, Q., Chen, Z., Mauceli, E., Hacohen, N., Gnirke, A., Rhind, N., di Palma, F., Birren, B. W., Nusbaum, C., Lindblad-Toh, K., Friedman, N., and Regev, A. (2011) Full-length transcriptome assembly from RNA-Seq data without a reference genome, *Nat. Biotechnol. 29*, 644–652.

50. Simão, F. A., Waterhouse, R. M., Ioannidis, P., Kriventseva, E. V., and Zdobnov, E. M. (2015) BUSCO: assessing genome assembly and annotation completeness with single-copy orthologs, *Bioinformatics 31*, 3210–3212.
51. Haas, B. J., Papanicolaou, A., Yassour, M., Grabherr, M., Blood, P. D., Bowden, J., Couger, M. B., Eccles, D., Li, B., Lieber, M., MacManes, M. D., Ott, M., Orvis, J., Pochet, N., Strozzi, F., Weeks, N., Westerman, R., William, T., Dewey, C. N., Henschel, R., LeDuc, R. D., Friedman, N., and Regev, A. (2013) De novo transcript sequence reconstruction from RNA-seq using the Trinity platform for reference generation and analysis, *Nat. Protoc. 8*, 1494–1512.
52. Priyam, A., Woodcroft, B. J., Rai, V., Munagala, A., Moghul, I., Ter, F., Gibbins, M. A., Moon, H., Leonard, G., Rumpf, W., and Wurm, Y. (2015) Sequenceserver: a modern graphical user interface for custom BLAST databases.
53. Mumberg, D., Müller, R., and Funk, M. (1995) Yeast vectors for the controlled expression of heterologous proteins in different genetic backgrounds, *Gene 156*, 119–122.
54. Lee, M. E., DeLoache, W. C., Cervantes, B., and Dueber, J. E. (2015) A Highly Characterized Yeast Toolkit for Modular, Multipart Assembly, *ACS Synth. Biol. 4*, 975–986.
55. Kumar, S., Stecher, G., and Tamura, K. (2016) MEGA7: Molecular Evolutionary Genetics Analysis Version 7.0 for Bigger Datasets, *Mol. Biol. Evol. 33*, 1870–1874.
56. Pluskal, T., Castillo, S., Villar-Briones, A., and Oresic, M. (2010) MZmine 2: modular framework for processing, visualizing, and analyzing mass spectrometry-based molecular profile data, *BMC Bioinformatics 11*, 395.
57. Schneider, C. A., Rasband, W. S., and Eliceiri, K. W. (2012) NIH Image to ImageJ: 25 years of image analysis, *Nat. Methods 9*, 671–675.
58. Kim, D. E., Chivian, D., and Baker, D. (2004) Protein structure prediction and analysis using the Robetta server, *Nucleic Acids Res. 32*, W526–31.
59. Vagin, A., and Teplyakov, A. (1997) MOLREP: an Automated Program for Molecular Replacement, *J. Appl. Crystallogr. 30*, 1022–1025.
60. Terwilliger, T. C., Grosse-Kunstleve, R. W., Afonine, P. V., Moriarty, N. W., Zwart, P. H., Hung, L. W., Read, R. J., and Adams, P. D. (2008) Iterative model building, structure refinement and density modification with the PHENIX AutoBuild wizard, *Acta Crystallogr. D Biol. Crystallogr. 64*, 61–69.
61. Murshudov, G. N., Skubák, P., Lebedev, A. A., Pannu, N. S., Steiner, R. A., Nicholls, R. A., Winn, M. D., Long, F., and Vagin, A. A. (2011) REFMAC5 for the refinement of macromolecular crystal structures, *Acta Crystallogr. D Biol. Crystallogr. 67*, 355–367.
62. Emsley, P., Lohkamp, B., Scott, W. G., and Cowtan, K. (2010) Features and development of Coot, *Acta Crystallogr. D Biol. Crystallogr. 66*, 486–501.

Graphic Table of Contents

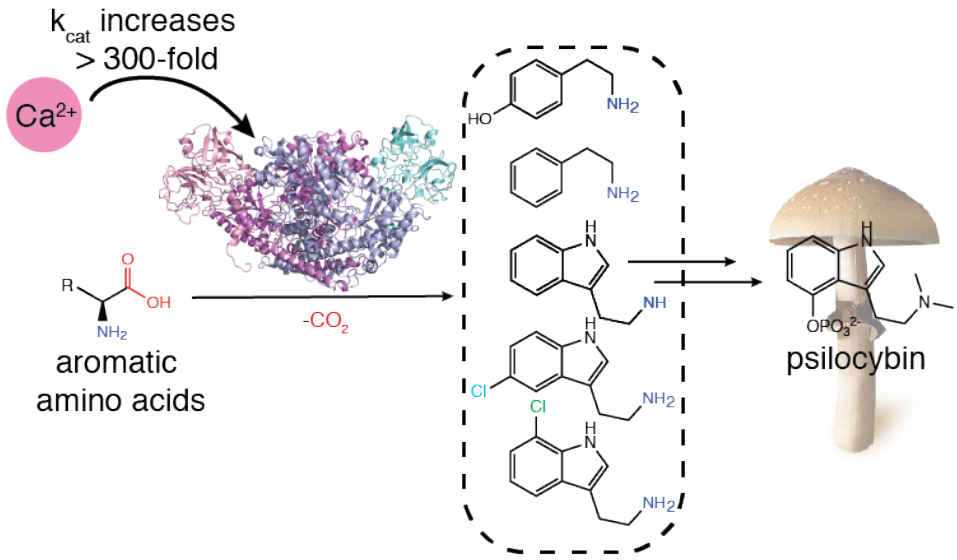

Supporting Information

Monoamine biosynthesis via a noncanonical calcium-activatable aromatic amino acid decarboxylase in *Psilocybe* mushroom

Michael P. Torrens-Spence[1†], Chun-Ting Liu[1,2,3†], Tomáš Pluskal[1], Yin Kwan Chung[1,4] and Jing-Ke Weng[1,2*]

[1]Whitehead Institute for Biomedical Research, 455 Main Street, Cambridge, MA 02142 USA.

[2]Department of Biology, Massachusetts Institute of Technology, Cambridge, MA 02139 USA.

[3]Department of Chemistry, Massachusetts Institute of Technology, Cambridge, MA 02139 USA.

[4]Division of Life Science, Hong Kong University of Science & Technology, Clear Water Bay, Hong Kong, China

† Co-first authors

*Corresponding author. Email: wengj@wi.mit.edu

Supplementary Tables

Table S1. Trinity ID of genes described in this study and their TPM values in the separately assembled fruiting-body and mycelium transcriptomes.

Gene	Trinity ID	TPM in fruiting body (ranking*)	TPM in mycelium (ranking*)
PcncAAAD	DN6739_c3_g2	530.52 (241)	11.02 (5168)
GAD1	DN5219_c0_g1	19.64 (5029)	55.45 (1391)
GAD2	DN6144_c0_g1	7.16 (7196)	10.67 (5241)
PcDHPAAS	DN2505_c0_g2; N2505_c0_g1	2.43 (9715)	0.54 (11627)
PsiD	DN5786_c0_g3	301.02 (465)	3.47 (7623)
PsiM	DN5702_c0_g1	191.82 (732)	10.58 (5270)
PsiK	DN5934_c1_g1	144.29 (971)	12.95 (4724)
PsiH	DN6531_c0_g1	212.67 (646)	26.92 (2769)

*Ranking among 13,672 expressed and assembled genes in both tissues. Number 1 being the most highly expressed gene.

Table S2. Crystallographic data collection and refinement statistics. Statistics for the highest-resolution shell are shown in parentheses.

	***Pc*ncAAAD**
Wavelength	0.9793 Å
Resolution range	71.79 - 1.97 (2.04 - 1.97)
Space group	C 1 2 1
Unit cell	238.723 143.57 71.408 90 92.775 90
Total reflections	1172077 (115473)
Unique reflections	168766 (16700)
Multiplicity	6.9 (6.9)
Completeness (%)	90.18 (74.75)
Mean I/sigma(I)	11.61 (1.12)
Wilson B-factor	31.22
R-merge	0.1437 (1.781)
R-meas	0.1554 (1.928)
R-pim	0.05863 (0.7294)
CC1/2	0.994 (0.567)
CC*	0.999 (0.851)
Reflections used in refinement	152529 (12617)
Reflections used for R-free	1811 (145)
R-work	0.1704 (0.2991)
R-free	0.1973 (0.3443)
CC(work)	0.962 (0.849)
CC(free)	0.951 (0.832)
Number of non-hydrogen atoms	16302
macromolecules	15261
ligands	70
solvent	252
Protein residues	1919
RMS(bonds)	0.011
RMS(angles)	1.28
Ramachandran favored (%)	97.27
Ramachandran allowed (%)	2.62
Ramachandran outliers (%)	0.10
Rotamer outliers (%)	0.72
Clashscore	7.08
Average B-factor	46.99
macromolecules	46.99
ligands	62.33
solvent	45.99

Table S3. Cloning primers used in this study.

Gene	Vector/ purpose	Direction	Sequence
*Pc*ncAAAD	pHis8-4	F	GAAAACTTGTACTTCCAGGCCCATGGCATGC CTTCCAGTCACCCTCACATTACTC
*Pc*ncAAAD	pHis8-4	R	CTCGAATTCGGATCCGCCATGGCTACTTCGTC GGAGCAACAGTCTCCAATTTG
*Pc*ncAAAD	p423TEF	F	GCATAGCAATCTAATCTAAGTTTTCTAGAACTA GTATGCCTTCCAGTCACCCTCAC
*Pc*ncAAAD	p423TEF	R	CAGCCCGGGGGATCCACTAGTCTACTTGGCG GGAGCGATAGTCTC
*Pc*GAD1	pHis8-4	F	GAAAACTTGTACTTCCAGGCCCATGGCATGG CGCTCTCCAAACACGTTAAC
*Pc*GAD1	pHis8-4	R	CTCGAATTCGGATCCGCCATGGTTAGCAAGG ACGAGCATAGGTTCCAC
*Pc*GAD1	p423TEF	F	GCATAGCAATCTAATCTAAGTTTTCTAGAACTA GTATGGCGCTCTCCAAACACGTTAAC
*Pc*GAD1	p423TEF	R	CAGCCCGGGGGATCCACTAGTTTAGCAAGGA CGAGCATAGGTTCCAC
*Pc*DHPAAS	pHis8-4	F	GAAAACTTGTACTTCCAGGCCCATGGCATGG ATATCGAACAATTTAGGAAAGCAGGC
*Pc*DHPAAS	pHis8-4	R	CTCGAATTCGGATCCGCCATGGCTATTCAGTG ATAGTTCCGTTGATAGTTTTCCAAGC
*Pc*DHPAAS	p423TEF	F	GCATAGCAATCTAATCTAAGTTTTCTAGAACTA GTATGGATATCGAACAATTTAGGAAAGCAGGC
*Pc*DHPAAS	p423TEF	R	CAGCCCGGGGGATCCACTAGTCTATTCAGTG ATAGTTCCGTTGATAGTTTTCCAAGC
PsiD	p423TEF	F	GCATAGCAATCTAATCTAAGTTTTCTAGAACTA G ATGCAGGTGATACCCGCGTG
PsiD	p423TEF	R	CAGCCCGGGGGATCCACTAGTCTAAGCCTTT AGAGCAGCGACGACTTC
RebH	pYTK001	F	GCATCGTCTCATCGGTCTCATATGTCAGGAAA GATCGACAAAATACTAATTGTGGG
RebH	pYTK001	R	ATGCCGTCTCAGGTCTCAGGATCTATCTTCCG TGTTGTTGACGTAAGAATTCATGTAAG

RebF	pYTK001	F	GCATCGTCTCATCGGTCTCATATGACAATCGAGTTTGACCGTCCAGG
RebF	pYTK001	R	ATGCCGTCTCAGGTCTCAGGATCTAGCCCTCTGGGGTCCAGAC
PyrH	pYTK001	F	GCATCGTCTCATCGGTCTCATATGATCCGTAGTGTTGTAATCGTCGGG
PyrH	pYTK001	R	ATGCCGTCTCAGGTCTCAGGATCTATTGGATGCTTGCAAGGTACTCGTAACA

Supplementary Figures

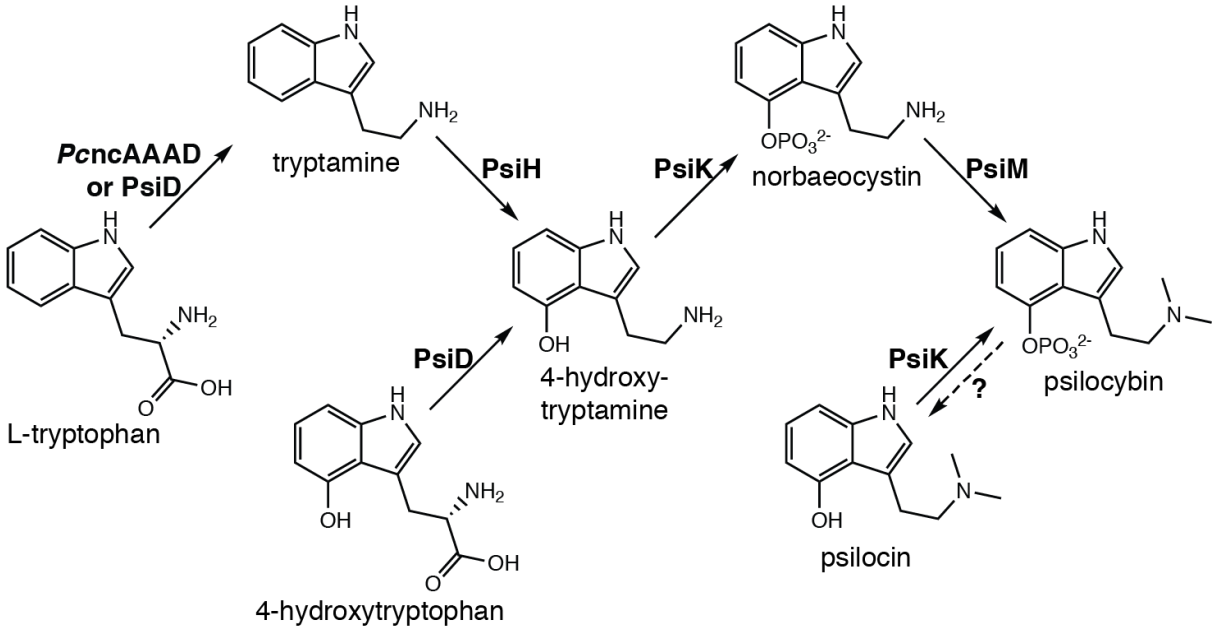

Figure S1. Biosynthetic pathway of psilocybin in *Psilocybe cubensis*. The enzymatic activities of PsiD, PsiH, PsiK, and PsiM have been previously reported, whereas the identity and function of *Pc*ncAAAD are reported in this study. The dotted arrow indicates potential intracellular dephosphorylation of psilocybin to form psilocin, where PsiK is suggested to provide a protective mechanism to re-phosphorylate the unstable psilocin (*1*). Figure adapted from ref 1.

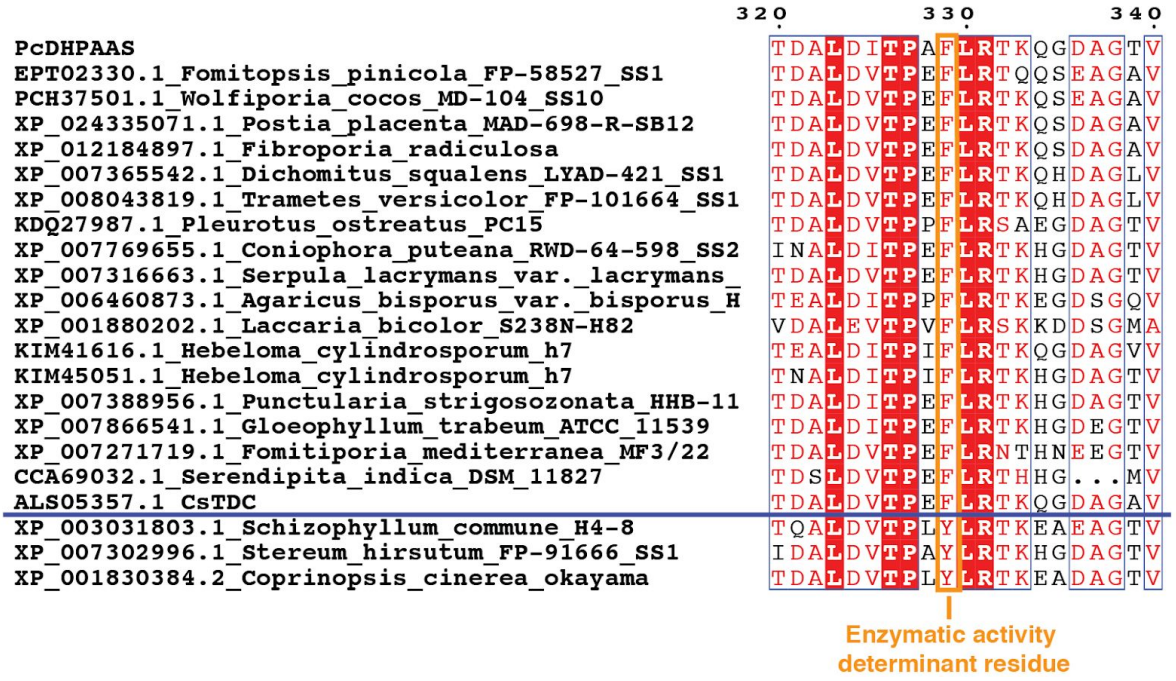

Figure S2. Residue 329 in *Pc*DHPAAS is the general enzymatic-activity-determining residue for type II PLP-dependent decarboxylases. According to previous studies (*2*, *3*), if this residue is a tyrosine, the enzyme performs decarboxylase chemistry, whereas bulky hydrophobic substitutions, such as phenylalanine, yield an enzyme with aldehyde synthase activity. Note that *Cs*TDC has a phenylalanine at this position, suggesting a different mechanism or mis-characterization of the enzyme.

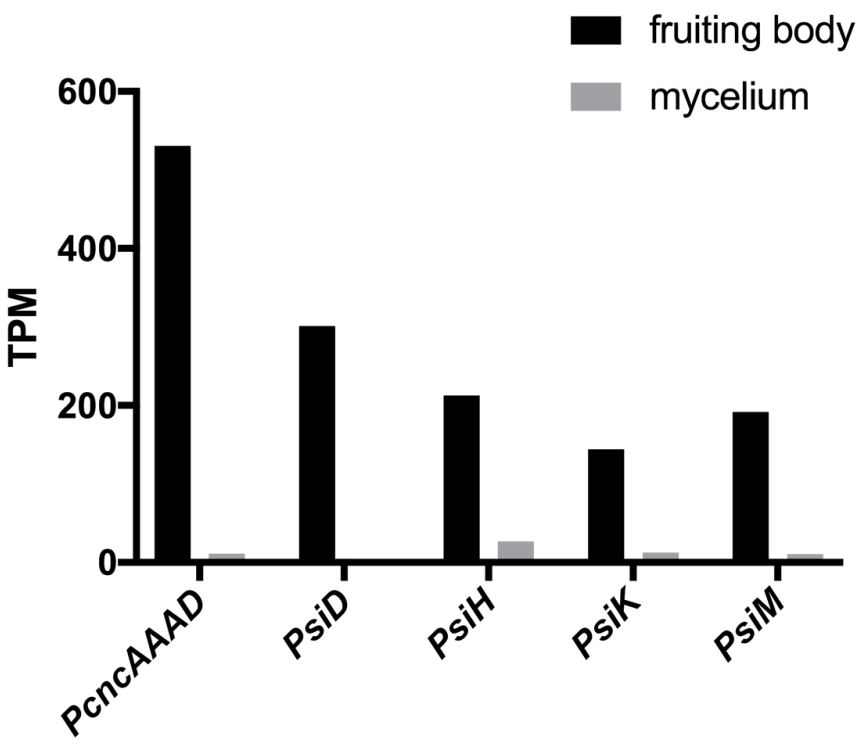

Figure S3. Relative expression levels of *PcncAAAD*, *PsiD*, *PsiH*, *PsiK*, and *PsiM* in the *P. cubensis* fruiting body and mycelium transcriptomes measured by transcript-per-million (TPM) values.

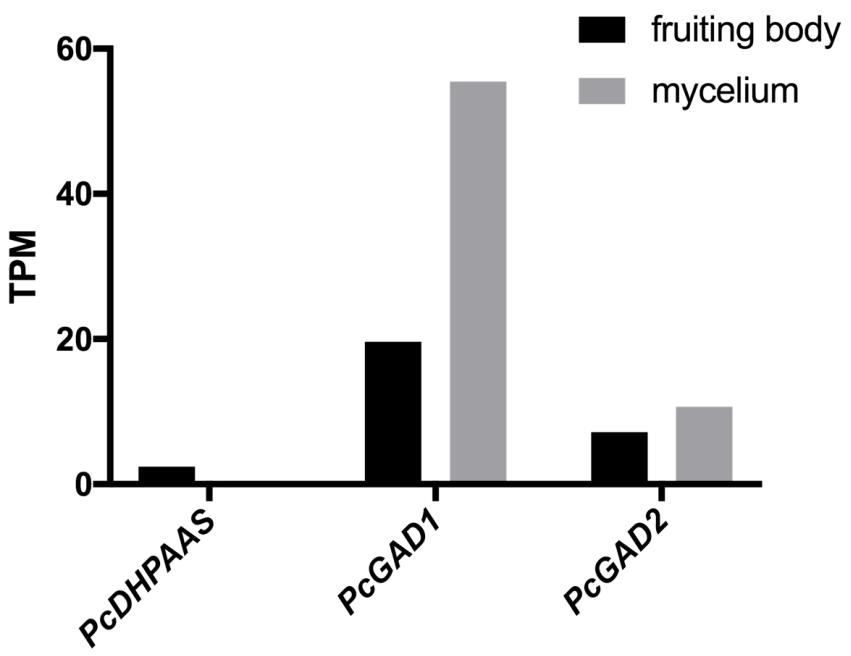

Figure S4. Relative expression levels of *PcDHPAAS* (a.k.a. *PcAAS* prior to the confirmation of its biochemical activity), *PcGAD1* and *PcGAD2* in the *P. cubensis* fruiting body and mycelium transcriptomes measured by transcript-per-million (TPM) values.

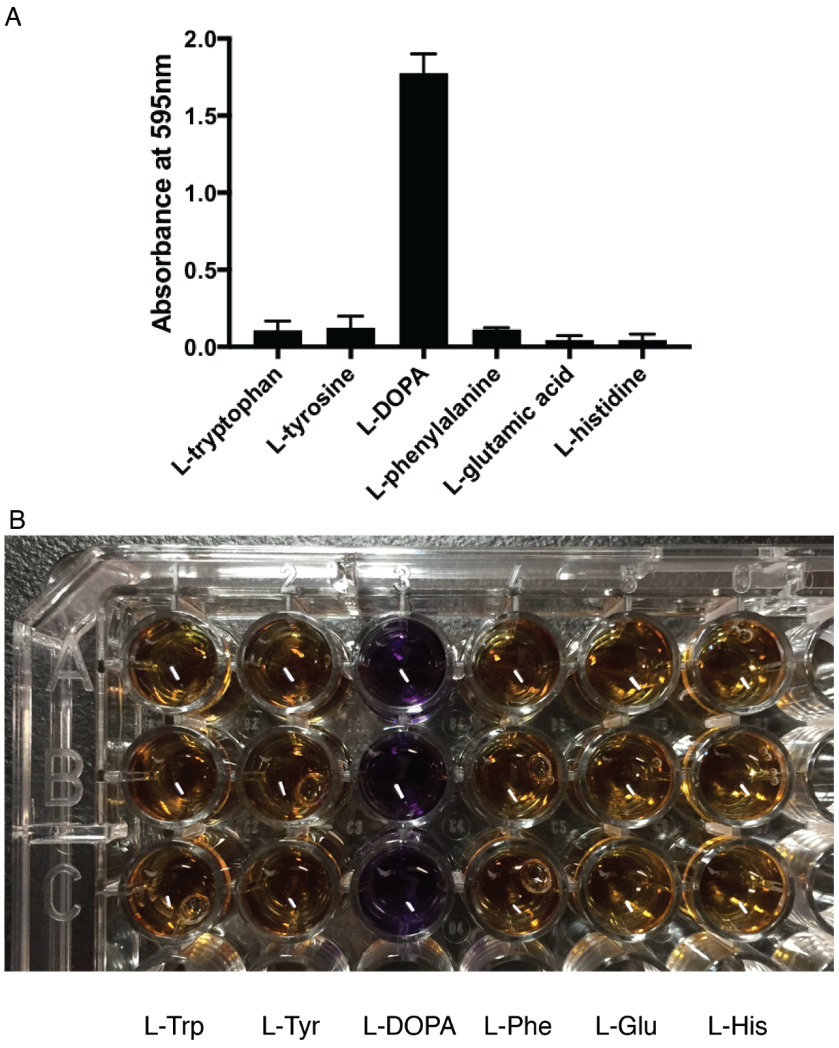

Figure S5. *Pc*AAS is a L-DOPA aldehyde synthase (*Pc*DHPAAS). (A) The aldehyde synthase activity of *Pc*DHPAAS was determined by measuring the co-product hydrogen peroxide. 200 µL of 50 mM potassium phosphate buffer (pH 7.5) containing 10 µg of recombinant *Pc*DHPAAS and 0.5 mM substrate were prepared in triplicate and incubated at 25 °C. The reactions were stopped after 10 minutes by addition of an equal volume of 0.8 M formic acid, and measured using the Pierce Quantitative Peroxide Assay Kit (Pierce) against a standard curve of hydrogen peroxide. Error bars represent standard error of the mean of the triplicate assays. (B) Picture of the hydrogen peroxide colorimetric assays. The purple color indicates hydrogen peroxide production.

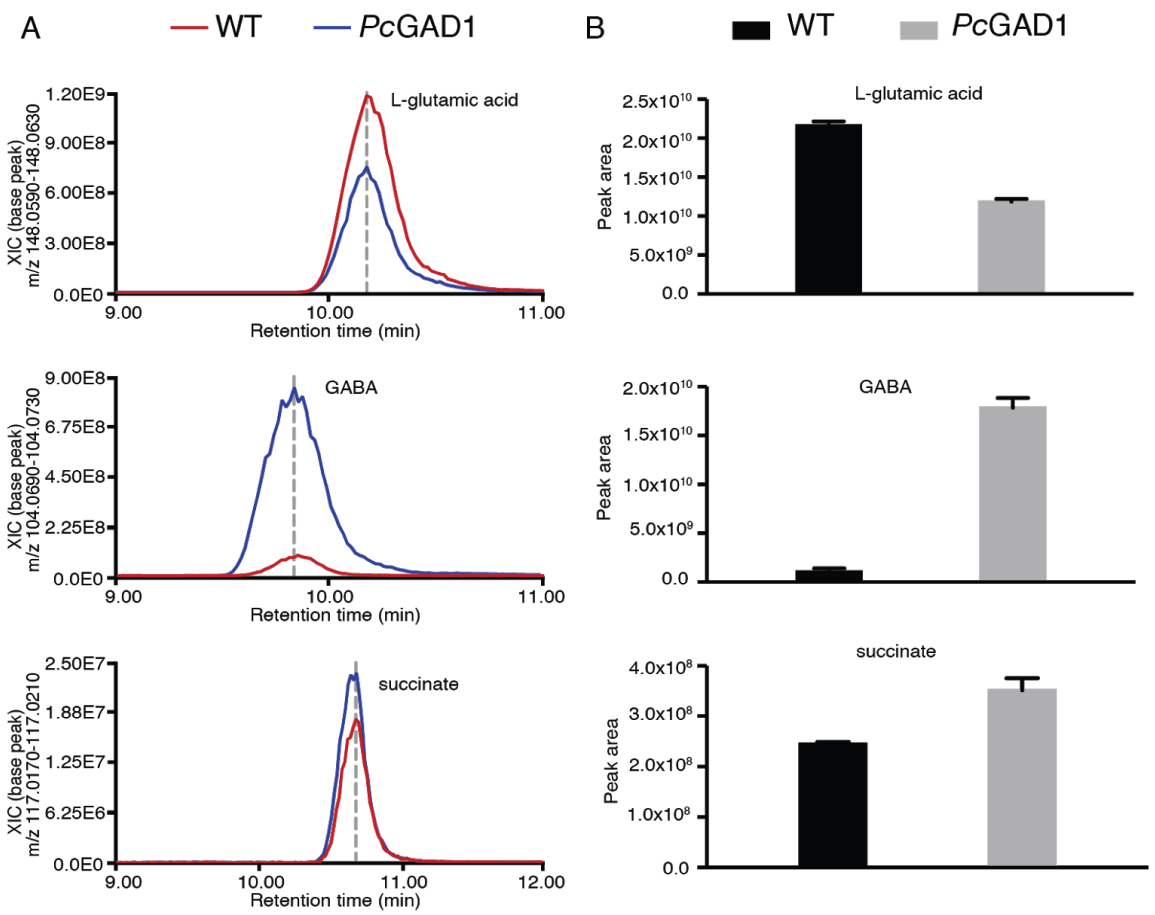

Figure S6. Transgenic yeast expressing *Pc*GAD1 was found to accumulate lower level of L-glutamic acid and higher levels of both GABA and its downstream catabolite succinate compared to the wild-type yeast (WT). (A) Chromatograms of the endogenous yeast metabolites L-glutamic acid, GABA and succinate. (B) Bar graphs illustrating the integrated peak area of L-glutamic acid, GABA and succinate. The black bars indicate the metabolite peak area in wild type yeast while the gray bar indicates peak area from *Pc*GAD1 expressing yeast. Error bars represent standard error of the mean of the biological triplicates. Metabolites were measured by LC-HRAM-MS and analyzed by MZmine2 (*4*).

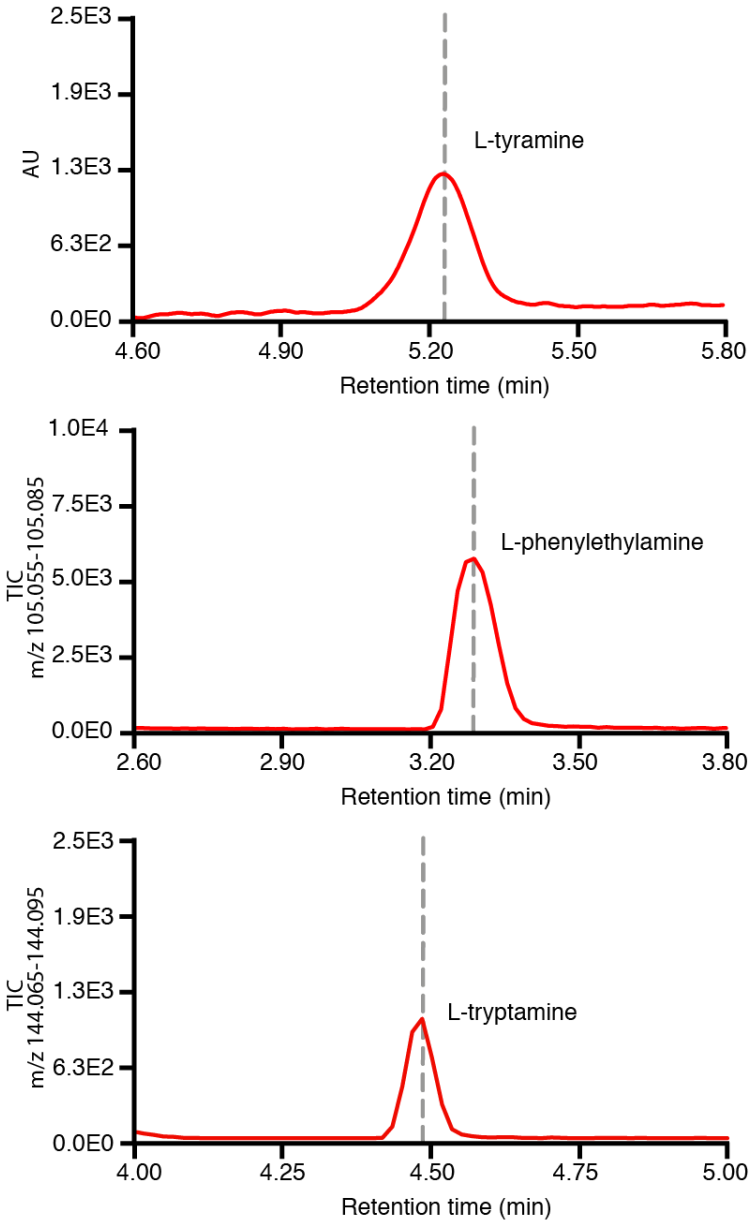

Figure S7. *In vitro* decarboxylation activity of *Pc*ncAAAD towards L-tyrosine, L-phenylalanine and L-tryptophan. The activities were measured by the production of the monoamines tyramine, tryptamine and phenylethylamine, respectively. Assays were conducted in a NaCl-containing reaction buffer at pH 8.0. Both phenylethylamine and tryptamine were measured by LC-MS, whereas tyramine was measured by LC-UV.

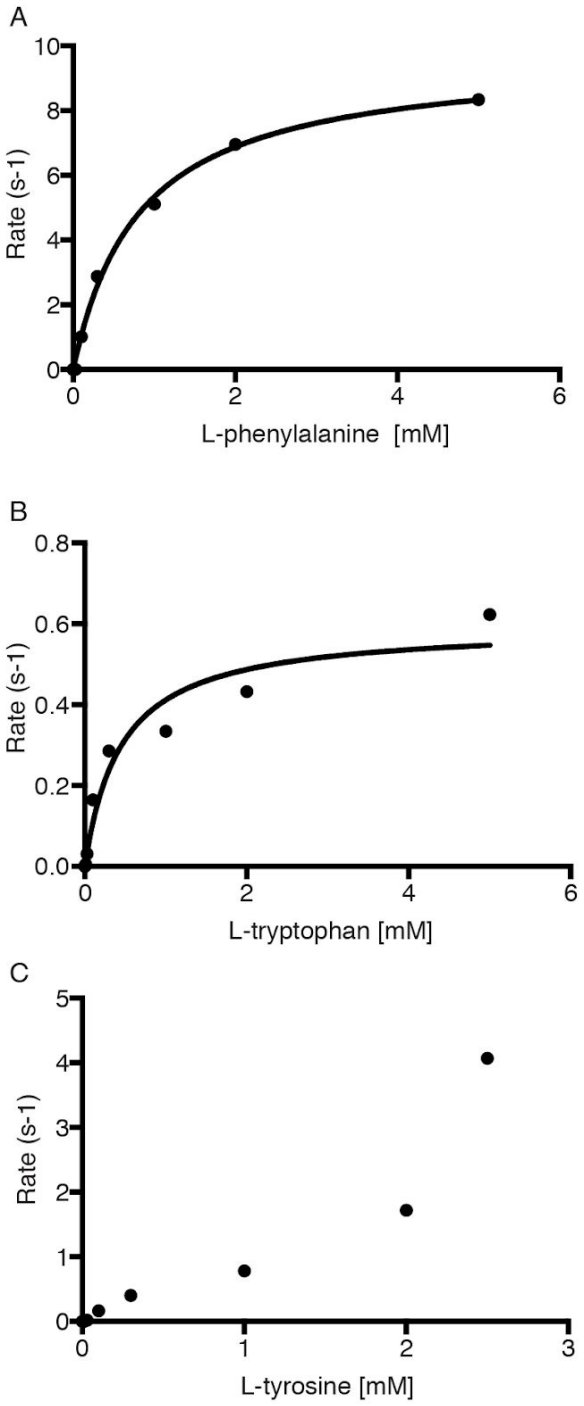

Figure S8. Kinetic characterization of *Pc*ncAAAD against L-phenylalanine, L-tryptophan and L-tyrosine in a reaction buffer containing 50 mM Tris pH 8.0 and 30 mM NaCl. Data collected for L-tyrosine could not be fitted to Michaelis-Menten curve by nonlinear regression for reasons discussed in the main text. The highest substrate concentration was 2.5 mM for L-tyrosine but 5 mM for both L-phenylalanine and L-tryptophan.

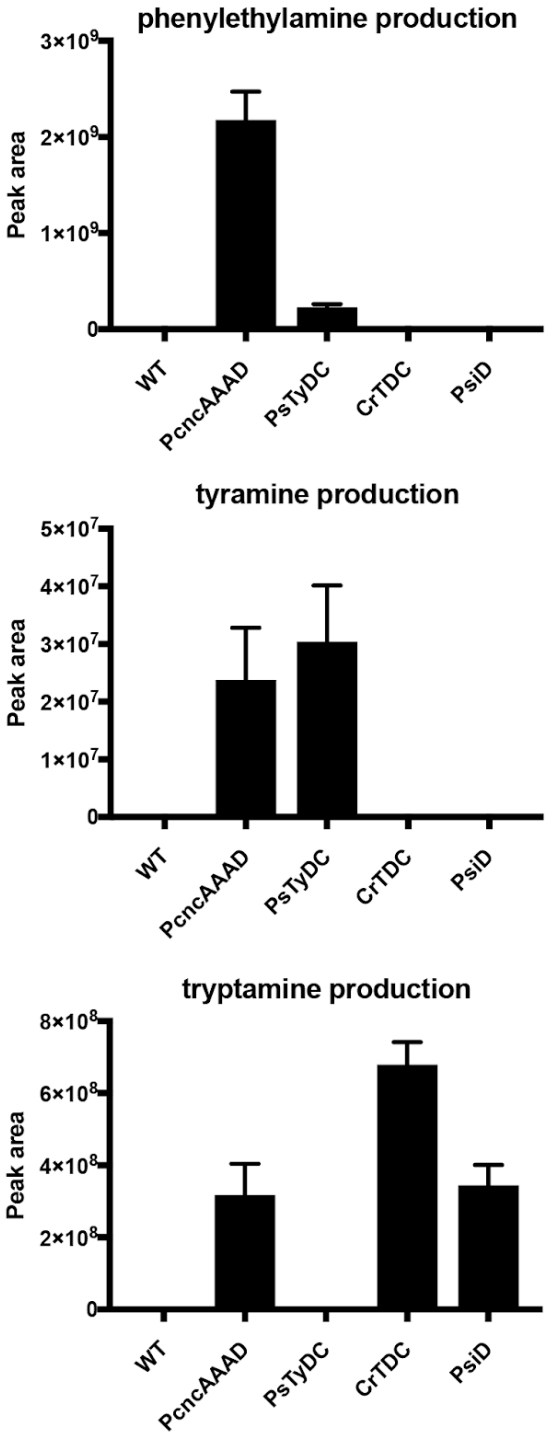

Figure S9. Relative activities of *Pc*ncAAAD, *Ps*TyDC, *Cr*TDC and PsiD towards various proteinogenic L-amino acid substrates measured in transgenic yeast. *S. cerevisiae* cultures were grown and analyzed by LC-HRAM-MS. Wild-type yeast (WT) was used as a negative control. Error bars represent standard error of the mean of the biological triplicates.

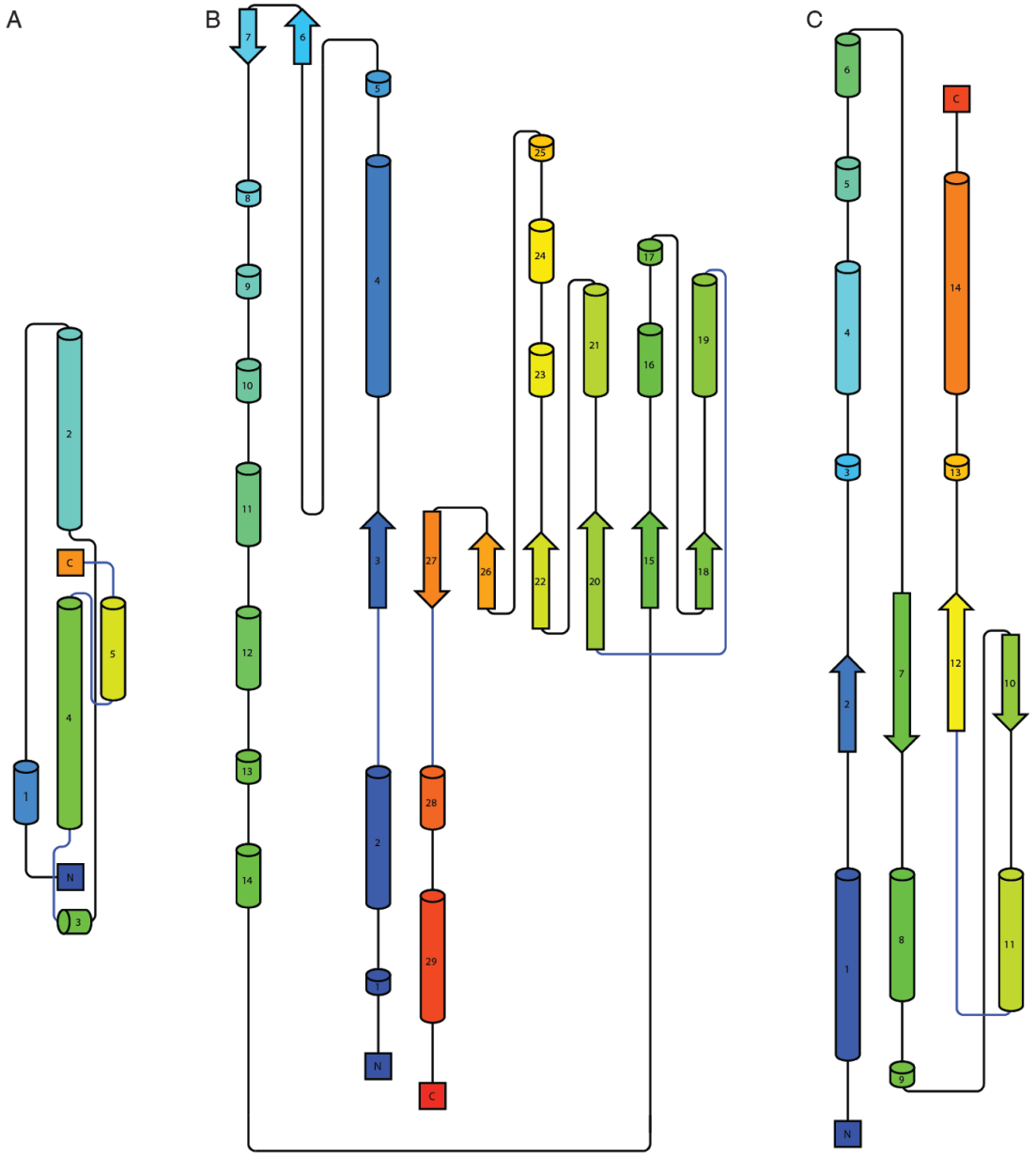

Figure S10. Topology diagrams of the three structural segments that constitute the *Pc*ncAAAD catalytic domain. Diagrams were generated using Pro-origami with secondary structure defined by DSSP (*5*). (A) Topology of the N-terminal segment (Val^{14} - Phe^{125}). (B) Topology of the middle or PLP-binding segment (Tyr^{126} - Gly^{511}). (C) Topology of the C-terminal segment (Tyr^{512} - Asp^{717}).

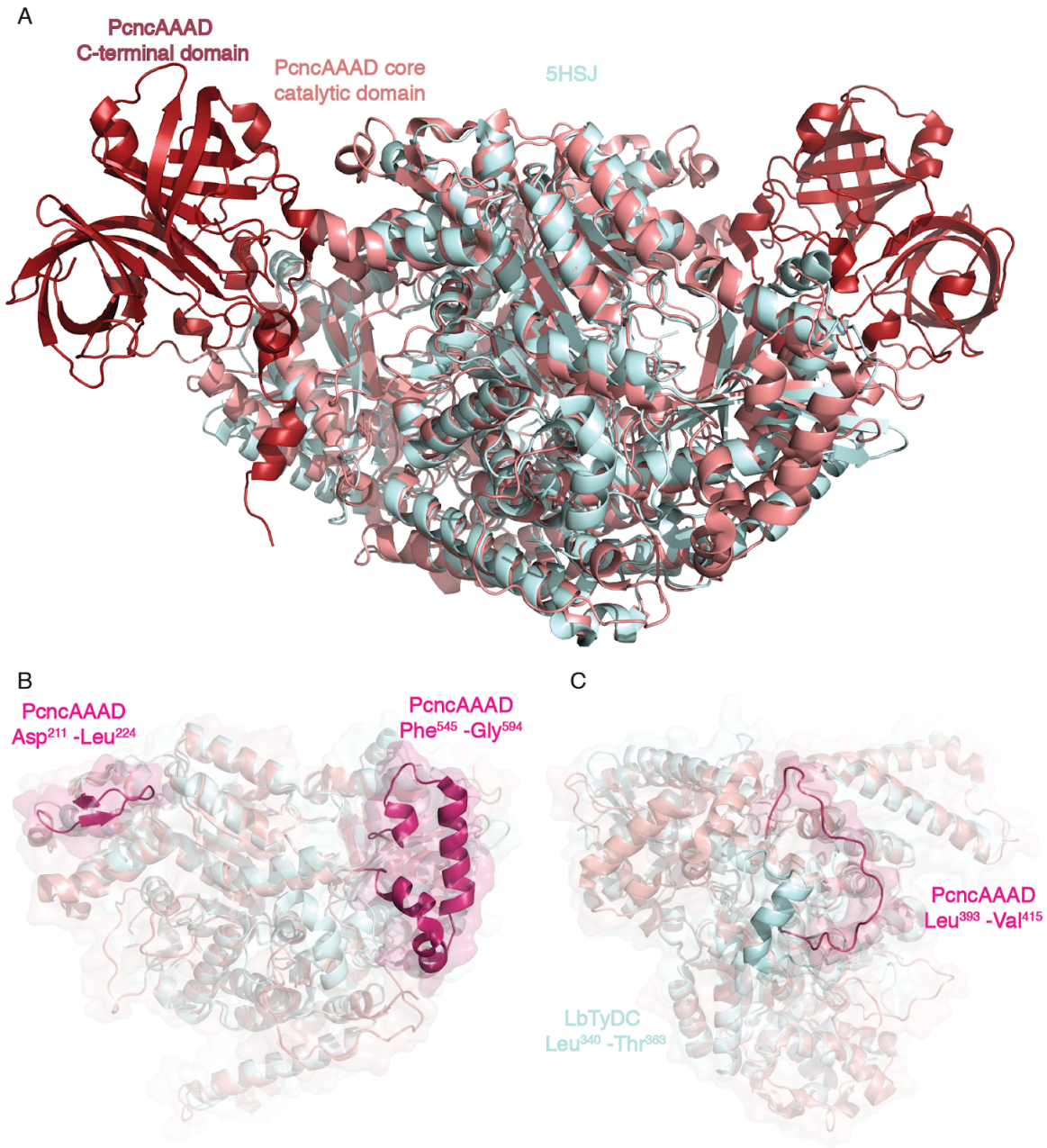

Figure S11. Superimposition of the *Pc*ncAAAD (PDB ID: 6EBN) and *Lb*TyDC (PDB ID: 5HSJ) structures. (A) The C-terminal appendage domains of the *Pc*ncAAAD homodimer is colored in fire brick red, and the core catalytic domains are colored in salmon. The *Lb*TyDC homodimer is colored in cyan. (B) Structure features unique to *Pc*ncAAAD. The inserted helixes relative to *Lb*TyDC are displayed in magenta, and the *Pc*ncAAAD core catalytic domain and a *Lb*TyDC monomer are colored in salmon and cyan, respectively. (C) Whereas Leu^{340} - Thr^{363} of *Lb*TyDC structure adopts a helix (cyan), the corresponding region (Leu^{393} - Val^{415}) in *Pc*ncAAAD forms a loop (magenta).

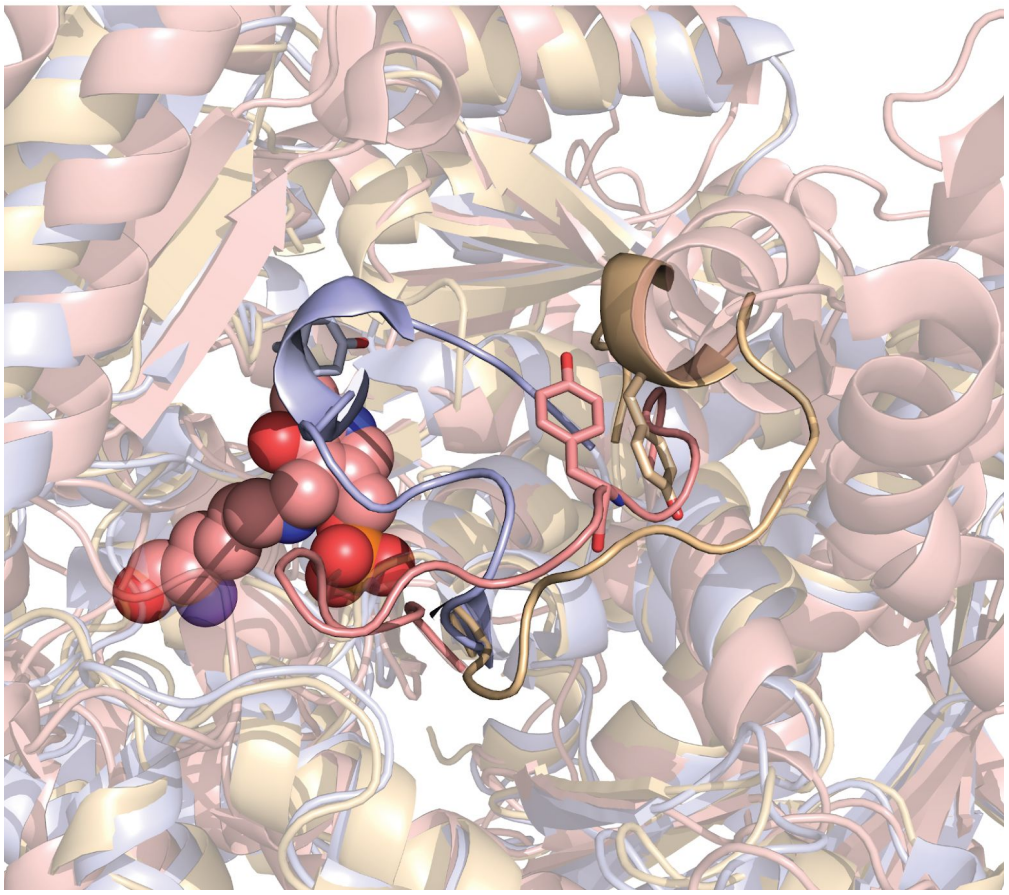

Figure S12. Superimposition of the *Hm*HDC (PDB ID: 4E1O), *Cr*TDC (PDB ID: 6EEW) and *Pc*ncAAAD (PDB ID: 6EBN) structures to illustrate the various conformation of the catalytic loop region. The *Pc*ncAAAD active-site LLP is displayed as spheres. The cartoon representation of *Hm*HDC, *Cr*TDC and *Pc*ncAAAD is colored in light blue, orange and salmon, respectively. The dynamic loops are emphasized in the foreground while the catalytic tyrosine from each structure are displayed as sticks.

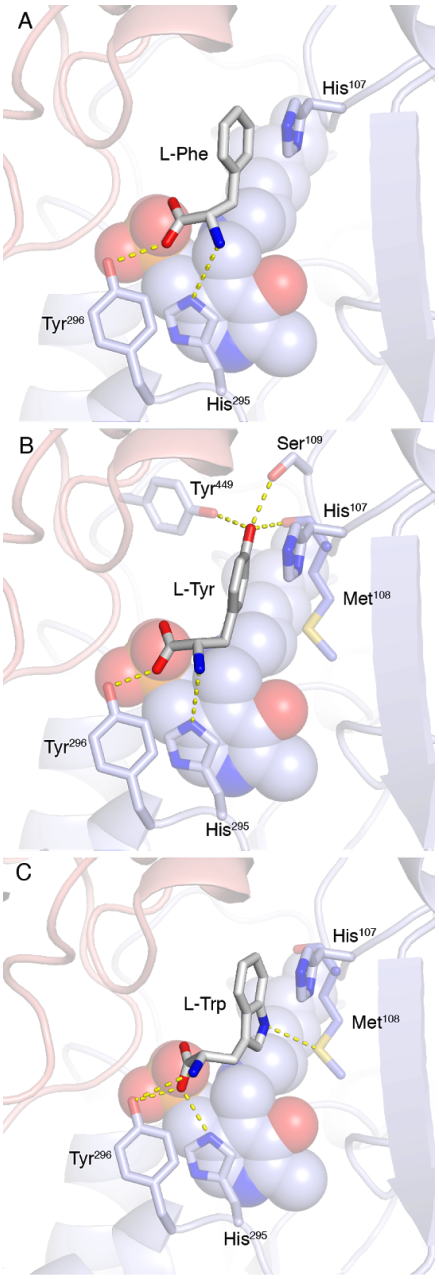

Figure S13. Modeled binding orientation of (A) L-phenylalanine, (B) L-tyrosine and (C) L-tryptophan in the *Pc*ncAAAD active site. The LLP is displayed as spheres, whereas residues putatively contributing to the binding of substrates are shown as sticks. *Pc*ncAAAD monomer A and B are shown in salmon and light blue, respectively. Simulated docking was performed using AutoDock Vina 1.1.2 (*6*). The binding affinity are -5.5, -6.1, and -6.1 kcal/mol for L-phenylalanine, L-tyrosine, and L-tryptophan docking models, respectively.

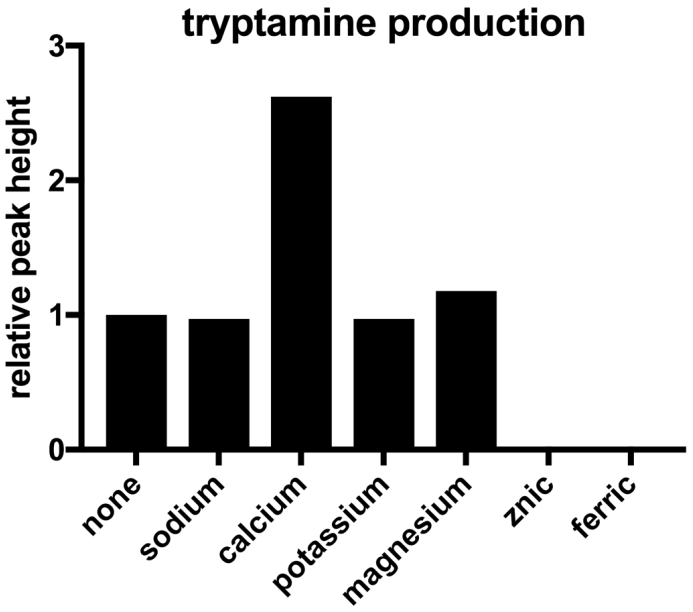

Figure S14. Relative tryptamine production of *Pc*ncAAAD in the presence of different metal ions measured by peak height. Tryptamine production of *Pc*ncAAAD in ion-free buffer is set to 1 in relative peak height. The reactions were carried out in 50 mM Tris buffer (pH 8.0) supplemented with 10 mM NaCl, $CaCl_2$, KI, $MgSO_4$, $ZnCl_2$, or $Fe(NO_3)_3$. Tryptamine levels were quantified by LC-MS. Tryptamine production was enhanced in the calcium-containing buffer, whereas other metal-containing buffers did not enhance *Pc*ncAAAD compared to the ion-free buffer.

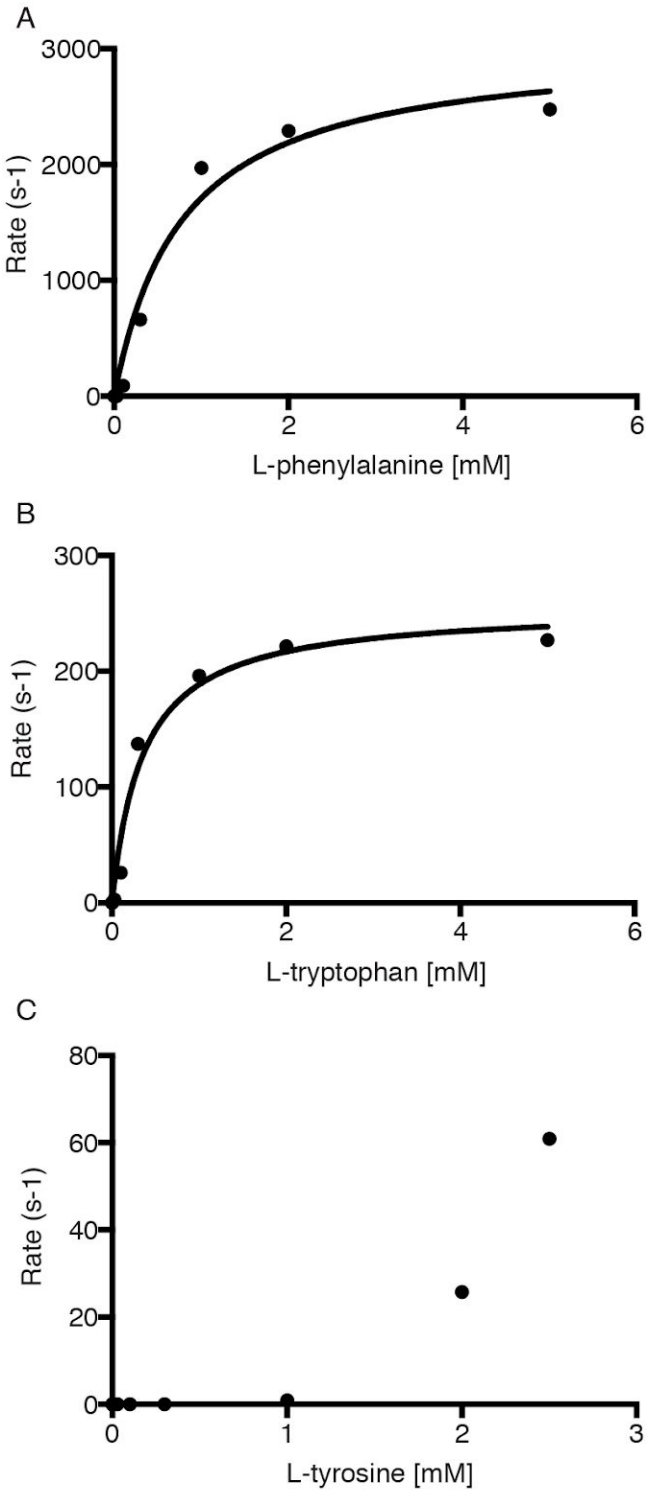

Figure S15. Kinetic characterization of *Pc*ncAAAD against L-phenylalanine, L-tryptophan and L-tyrosine in a reaction buffer containing 50 mM Tris pH 8.0 and 30 mM calcium acetate. Data collected for L-tyrosine could not be fitted to Michaelis-Menten curve by nonlinear regression for reasons discussed in the main text. The highest substrate concentration tested for L-tyrosine 2.5 mM while L-phenylalanine and L-tryptophan were assayed up to 5mM.

Supplementary references

1. Fricke, J., Blei, F., and Hoffmeister, D. (2017) Enzymatic Synthesis of Psilocybin, *Angew. Chem. Int. Ed Engl. 56*, 12352–12355.
2. Torrens-Spence, M. P., Liu, P., Ding, H., Harich, K., Gillaspy, G., and Li, J. (2013) Biochemical evaluation of the decarboxylation and decarboxylation-deamination activities of plant aromatic amino acid decarboxylases, *J. Biol. Chem. 288*, 2376–2387.
3. Torrens-Spence, M. P., Chiang, Y.-C., Smith, T., Vicent, M. A., Wang, Y., and Weng, J.-K. (2018) Structural basis for independent origins of new catalytic machineries in plant AAAD proteins.
4. Pluskal, T., Castillo, S., Villar-Briones, A., and Oresic, M. (2010) MZmine 2: modular framework for processing, visualizing, and analyzing mass spectrometry-based molecular profile data, *BMC Bioinformatics 11*, 395.
5. Stivala, A., Wybrow, M., Wirth, A., Whisstock, J. C., and Stuckey, P. J. (2011) Automatic generation of protein structure cartoons with Pro-origami, *Bioinformatics 27*, 3315–3316.
6. Trott, O., and Olson, A. J. (2010) AutoDock Vina: improving the speed and accuracy of docking with a new scoring function, efficient optimization, and multithreading, *J. Comput. Chem. 31*, 455–461.